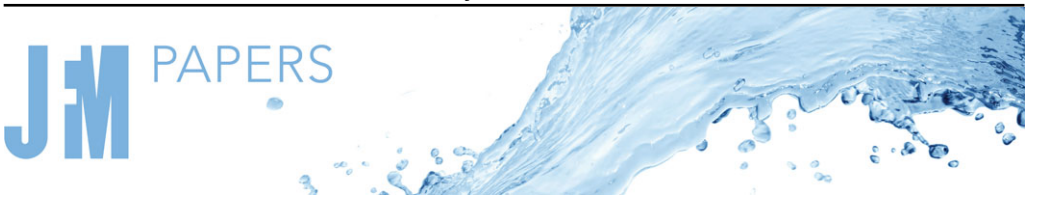
J. Fluid Mech. (2025), *vol.* 1008, A51, doi:10.1017/jfm.2025.199



Optimal growth in hypersonic flows over an inclined cone

Xi Chen[1], **Bingbing Wan**[1], **Guohua Tu**[1], **Maochang Duan**[1], **Xiaohu Li**[1] **and Jianqiang Chen**[1]

[1]State Key Laboratory of Aerodynamics, Mianyang, Sichuan 621000, PR China

Corresponding authors: Bingbing Wan, wanbing@tju.edu.cn; Jianqiang Chen, chenjq@cardc.cn

(Received 22 June 2024; revised 8 December 2024; accepted 10 February 2025)

Spatial optimal responses to both inlet disturbances and harmonic external forcing for hypersonic flows over a blunt cone at non-zero angles of attack are obtained by efficiently solving the direct–adjoint equations with a parabolic approach. In either case, the most amplified disturbances initially take the form of localised streamwise vortices on the windward side and will undergo a two-stage evolution process when propagating downstream: they first experience a substantial algebraic growth by exploiting the Orr and lift-up mechanisms, and then smoothly transition to a quasi-exponential growth stage driven by the crossflow-instability mechanism, accompanied by an azimuthal advection of the disturbance structure towards the leeward side. The algebraic growth phase is most receptive to the external forcing, whereas the exponential growth stage relies on the disturbance frequency and can be significantly strengthened by increasing the angle of attack. The wavemaker delineating the structural sensitivity region for the optimal gain is shown to lie on the windward side immediately downstream of the inlet, implying a potent control strategy. Additionally, considerable non-modal growth is also observed for broadband high-frequency disturbances residing in the entropy layer.

Key words: boundary layer stability, hypersonic flow, shear-flow instability

1. Introduction

Hypersonic vehicles are faced with three-dimensional (3-D) boundary-layer transition problems that yield an undesirable increase in heat flux and skin friction. In contrast to the two-dimensional (2-D) boundary layer over a flat plate, cone at zero degrees angle of attack, etc., the 3-D counterpart features non-uniform pressure distribution in the azimuthal direction, and as such exhibits three distinct regions across the vehicle surfaces, i.e. the attachment-line region (high-pressure region), the vortex region (low-pressure

© The Author(s), 2025. Published by Cambridge University Press.

https://doi.org/10.1017/jfm.2025.199 Published online by Cambridge University Press

region) and the crossflow region in between. Each region sustains certain modal instabilities likely responsible for the boundary-layer breakdown. Of particular interest is the crossflow region where boundary-layer transition is generally dominated by crossflow instabilities comprising stationary and travelling modes (Reed & Saric 1989) and occurs over the largest part of the vehicle surface.

Base flow in the crossflow region varies mildly in the azimuthal direction, which appears amenable to one-dimensional (1-D) stability analyses. To obtain the evolution of crossflow vortices, it is common practice to first model a vortex path and the azimuthal wavenumber variation along the path, and then integrate the (nonlinear) parabolised stability equations (PSEs) assuming azimuthal periodicity (Kocian *et al.* 2019; Song *et al.* 2020). However, the 1-D tools find it difficult to model the typical wavepacket structures of the crossflow mode, and also can not deal with the nonlinear interactions between multiple modes as local modes may have different trajectories. Therefore, one attempts to establish a multi-dimensional stability analysis framework to delineate the crossflow instability behaviour in a 3-D boundary layer. Paredes *et al.* (2016*b*) and later Lakebrink *et al.* (2017) adopted 2-D local linear stability theory (LST; sometimes termed the BiGlobal approach) solving 2-D eigenvalue equations to uncover the modal structure of the travelling crossflow instability over an elliptic cone. They found that the shape function of the crossflow mode exhibits rapid oscillations in the azimuthal direction and covers almost the entire surface of the vehicle, thus requiring a large number of grid points to resolve. In a similar study of a lifting body, Chen *et al.* (2022) documented that the 2-D local crossflow modal eigenvalues are too sensitive to azimuthal resolution to be grid converged. This extreme sensitivity of eigenvalues, on the one hand, reflects the highly non-orthogonal nature of the linear operator and, on the other hand, is physically due to the weakly non-parallel effects (i.e. the azimuthal wavelength of the crossflow mode is much smaller compared with the azimuthal variation scale of the base flow) (Chomaz 2005), analogous to previous studies on the streamwise BiGlobal problem (e.g. Åkervik *et al.* 2008). They also showed that the global spectrum for a single frequency contains many unstable modes without a predominant one, which was reported by Liu *et al.* (2022*a*) as well in studying an inclined cone configuration. The poor grid convergence of eigenvalues and the multiplicity of crossflow modes make the interpretation of global/2-D local modal instability results challenging. As a result, the 2-D local modal stability analysis may be unable to properly describe the crossflow instability in a complex 3-D boundary layer. Furthermore, it has become increasingly evident that modal instability analysis alone cannot explain all transition phenomena, as exemplified by the famous blunt-cone paradox concerning subcritical transition on a large-bluntness cone (Reshotko & Tumin 2000). Recently, Paredes *et al.* (2023) and Chen *et al.* (2024) who investigated the leeward modal instabilities of hypersonic flow over yawed blunt cones both identified strikingly low N-factors (below 2) correlated with the observed transition location, pointing to unknown transition mechanisms.

The alternative approach is based on the non-modal stability analysis framework which considers the non-modal combinations of multiple modes simultaneously (Schmid & Henningson 2001; Schmid 2007). Instead of focusing on the modal instability, the non-modal stability analysis aims to identify the most dangerous case from all potential routes of disturbance evolution, which is important since inlet conditions are typically unavailable in realistic situations. Moreover, the optimal solution proves to be robust to small perturbations even if the eigenvalues may not (Reddy *et al.* 1993; Schmid 2007). The non-modal stability analysis can be conducted in the temporal domain (temporal approach) seeking the intrinsic disturbances in the flow field that result in the maximal energy growth over a certain time interval, or in the frequency domain (spatial approach)

https://doi.org/10.1017/jfm.2025.199 Published online by Cambridge University Press

finding the optimal disturbances that achieve the largest spatial growth. In the spatial growth analysis, the input/output disturbances/forcings can be anywhere within the flow field (often termed the input–output/resolvent (I-O) analysis; see Jovanović & Bamieh (2005)) or be restricted to the inlet and outlet only (conventional optimal growth analysis). In this work, we compute a frequency domain problem for time-harmonic disturbances to retrieve optimal disturbances with such two types of choices on the input and output domains.

The early non-modal stability analyses were mostly conducted for simple shear flows (Poiseuille flow, Couette flow, Blasius boundary layer, etc.) in the low-speed regime, showing that disturbances can be considerably (linearly) amplified through the Orr mechanism and lift-up effect even if they are modally stable (Schmid & Henningson 2001). The Orr mechanism is predominant for 2-D waves and relies on the deformation of vorticity patches under the action of the base flow. The deformation reduces the support area of the vorticity such that the vorticity extrema increase owing to the Kelvin circulation preservation theorem, thereby causing a transient energy growth (Nastro *et al.* 2020). The lift-up effect corresponds to the emergence of streaks induced by streamwise vortices. In general, 3-D optimal perturbation combines these mechanisms in a synergistic manner in which the cross-stream velocity produced by the Orr mechanism enhances the streamwise rolls associated with streak production (Farrell & Ioannou 1993). The optimal perturbation can sometimes initiate the modal instability, especially in 3-D boundary layers where modal and non-modal growths are observed for similar disturbance structures. Corbett & Bottaro (2001) who studied temporal optimal disturbances in Falkner–Skan–Cooke flow modelling the boundary layer over an infinite swept wing found that these initially take the form of vortices which are almost aligned with the external streamline and evolve into crossflow modes downstream. They argued that non-modal growth may provide proper initial conditions for modal growth and thus constitutes a preferential receptivity path for the selection of exponential instabilities in 3-D boundary layers. For a similar configuration, Tempelmann *et al.* (2010) utilised a spatial approach based on the method of Lagrange multipliers and PSEs to reveal that the optimal disturbance manifests as streamwise vortices aligned against the crossflow, extracts energy by leveraging both the Orr and lift-up mechanisms and develops smoothly into crossflow modes downstream. They (Tempelmann *et al.* 2012) later extended the study to compressible flow (up to Mach 1.5), showing that optimal growth increases for higher Mach numbers and wall cooling destabilises disturbances of non-modal nature. Nonetheless, the physical mechanisms of optimal growth in compressible boundary layers are found to be similar to those in the incompressible counterpart.

The first non-modal stability analysis in compressible flow comes from Hanifi *et al.* (1996) who, adopting the temporal approach, examined the effects of different parts of spectra on the optimal growth, and obtained similar optimal structures to those in incompressible flow. Their work was later complemented by a spatial study performed by Tumin & Reshotko (2003). Laible & Fasel (2016) identified a constantly non-modal growth mechanism in the streamwise development of the streak mode in oblique breakdown, by which the streak mode retains a higher amplitude level than other nonlinearly generated modes. Paredes *et al.* (2019, 2020) observed substantial non-modal growth of disturbances peaking within the entropy layer around the nose of a blunt cone, and furthermore showed that such disturbances could trigger the boundary-layer transition through oblique breakdown.

The aforementioned studies considered essentially 2-D compressible boundary layers where the flow field is treated as homogeneous in at least one direction (usually the azimuthal/spanwise direction). Non-modal analyses of truly 3-D compressible boundary

https://doi.org/10.1017/jfm.2025.199 Published online by Cambridge University Press

layers are rare. Cook *et al.* (2020) obtained the optimal response of a hypersonic finned-cone boundary layer to wall roughnesses by partitioning the entire domain into smaller segments and progressively solving the I-O equations of each segment. Paredes *et al.* (2022) calculated the optimal disturbances for flow field around an isolated 3-D roughness with harmonic linearised Navier–Stokes (HLNS) equations, emphasising the importance of the disturbance amplification in the backward-flow region of the roughness. The above two studies both entail iteratively solving large-scale linear systems with unknowns at an order of one million, which is prohibitively expensive especially for a parametric study. Quintanilha *et al.* (2022) performed a temporal non-modal stability analysis on an elliptic-cone boundary layer under hypersonic flight conditions. They observed a strong transient growth in the crossflow region, which is strengthened with increasing flight altitude and as such is likely the important mechanism responsible for the high-altitude boundary-layer transition. In their study, the optimal disturbance is constructed by a linear combination of a finite number of 2-D local modes whose amplitude coefficients are optimised to achieve the maximum amplification at a given time horizon. Their results may, however, be compromised by the aforementioned high sensitivity of 2-D local crossflow modes, as well as the partial consideration of the eigenvalue spectrum (Bagheri *et al.* 2009) since obtaining the entire spectrum is infeasible. Moreover, the spatial optimal growth mechanisms pertaining to crossflow disturbances in a truly 3-D boundary layer remain hitherto insufficiently understood.

In the present study, we aim at establishing a proper description of the crossflow instabilities from a multi-dimensional perspective with the help of non-modal analysis, and furthermore elucidating the optimal growth mechanisms for a prototypical 3-D boundary layer. To this end, we attempt to constitute an efficient and accurate spatial optimal growth calculation framework based on a parabolic set of equations, and employ it to systematically study the optimal responses over a hypersonic inclined cone to both inlet perturbation and external forcings, with a special focus on the influence of the angle of attack (AoA). The related methodologies are summarised in § 2. Then, the linear non-modal characteristics of the selected configuration are presented in § 3, followed by discussions on the effects of AoA in § 4. Finally, concluding remarks and discussions are given in § 5.

2. Numerical set-up and linear stability theories

The numerical simulation and stability analysis are based on the equations of ideal gas flow written in dimensionless form as

$$\frac{\partial \rho}{\partial t} + \boldsymbol{\nabla} \cdot (\rho \boldsymbol{V}) = 0, \tag{2.1}$$

$$\rho \left[\frac{\partial \boldsymbol{V}}{\partial t} + (\boldsymbol{V} \cdot \boldsymbol{\nabla}) \boldsymbol{V} \right] = -\boldsymbol{\nabla} P + \frac{1}{R} \boldsymbol{\nabla} \cdot \left[\mu (\boldsymbol{\nabla} \boldsymbol{V} + \boldsymbol{\nabla} \boldsymbol{V}^t + l_0 \boldsymbol{\nabla} \cdot \boldsymbol{V} \mathbf{I}) \right], \tag{2.2}$$

$$\begin{aligned} \rho \left[\frac{\partial T}{\partial t} + (\boldsymbol{V} \cdot \boldsymbol{\nabla}) T \right] &= (\gamma - 1) M_\infty^2 \left[\frac{\partial P}{\partial t} + (\boldsymbol{V} \cdot \boldsymbol{\nabla}) P \right] + \frac{1}{R\, Pr} \boldsymbol{\nabla} \cdot (\kappa \boldsymbol{\nabla} T) \\ &+ \frac{(\gamma - 1) M_\infty^2 \mu}{2R} \left(\boldsymbol{\nabla} \boldsymbol{V} + \boldsymbol{\nabla} \boldsymbol{V}^t + l_0 \boldsymbol{\nabla} \cdot \boldsymbol{V} \mathbf{I} \right) : \left(\boldsymbol{\nabla} \boldsymbol{V} + \boldsymbol{\nabla} \boldsymbol{V}^t + l_0 \boldsymbol{\nabla} \cdot \boldsymbol{V} \mathbf{I} \right), \end{aligned} \tag{2.3}$$

where $\boldsymbol{V} = (U, V, W)$ is the velocity vector, $\mathbf{I}$ the identity tensor, ρ the density, P the pressure, T the temperature, M_∞ the Mach number, R the Reynolds number, $Pr = 0.7$ the Prandtl number, $\gamma = 1.4$ the specific heat coefficient, κ the thermal conductivity and μ the first coefficient of viscosity. The reference values of velocity and temperature are

https://doi.org/10.1017/jfm.2025.199 Published online by Cambridge University Press

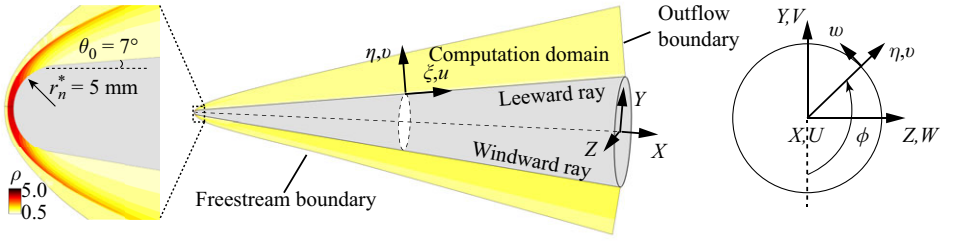


Figure 1. Sketch of the flow configuration and the computation domain for the base-flow calculation with the density distribution (for the case of 2° AoA) showing the shock position. The velocity components (U, V, W) in Cartesian coordinates (X, Y, Z) and velocity components (u, v, w) in body-oriented coordinates (ξ, η, ϕ) are also shown.

the corresponding values at the free stream with the subscript $()_\infty$. The reference value for pressure is $\rho_\infty U_\infty^2$. The equation of state is $p = \rho T/(\gamma M_\infty^2)$. The Stokes law $l_0 = -2/3$ has been assumed and the viscosity coefficient is estimated by Sutherland's law:

$$\mu = T^{3/2}\frac{1 + Cs}{T + Cs}, \tag{2.4}$$

with $Cs = 110.4\ \mathrm{K}/T_\infty^*$ for air in standard conditions. Dimensional variables are denoted with the superscript $()^*$.

2.1. *Model*

The model currently being studied is a 7°-half-angle (θ_0) blunt cone at AoA of 2°, 4° and 6°. The model is 900 mm long and has a nose radius of 5 mm. The free-stream Mach number $M_\infty = 6$, unit Reynolds number $Re_\infty^* = 4 \times 10^7\ \mathrm{m}^{-1}$, free-stream static temperature $T_\infty^* = 61.1$ K and wall temperature $T_w^* = 300$ K. The flow configuration is sketched in figure 1. The transformation relationship between the body-oriented coordinates and the Cartesian coordinates is as follows:

$$X = \xi\cos(\theta_0) - \eta\sin(\theta_0), \quad Y = -\tilde{\eta}\cos(\phi), \quad Z = \tilde{\eta}\sin(\phi), \tag{2.5}$$

where $\tilde{\eta} \equiv \xi\sin(\theta_0) + \eta\cos(\theta_0)$. All flow quantities are non-dimensionalised using the reference length $L^* = 0.0387$ mm (the boundary-layer scale at $X^* = 10$ mm), the free-stream velocity, density and temperature.

2.2. *Base-flow calculations*

A well-validated in-house code (Zhao 2017; Wan *et al.* 2018) was used to solve the unsteady compressible Navier–Stokes equations. The grid resolution is $N_\xi \times N_\eta \times N_\phi = 501 \times 301 \times 301$ for the first two cases and $N_\xi \times N_\eta \times N_\phi = 751 \times 301 \times 361$ for the last case (6° AoA), where N_ξ, N_η, N_ϕ is the number of grid points in the streamwise, wall-normal and azimuthal directions, respectively. The grid is stretched in the wall-normal and streamwise directions so that sufficient (at least 100) points are in the boundary layer and in the vicinity of the nose part, and is furthermore aligned with the leading-edge shock to diminish the numerical oscillations from the shock layer. Only half of the flow field is simulated by exploiting the azimuthal symmetry. The inviscid fluxes are computed by using a third-order WENO scheme, while the viscous fluxes are discretised using a fourth-order central-difference scheme. The time integration is performed using a third-order Runge–Kutta scheme. The upper boundary lies outside the shock, where the oncoming flow quantities are specified. At the outflow boundary, a third-order extrapolation boundary

https://doi.org/10.1017/jfm.2025.199 Published online by Cambridge University Press

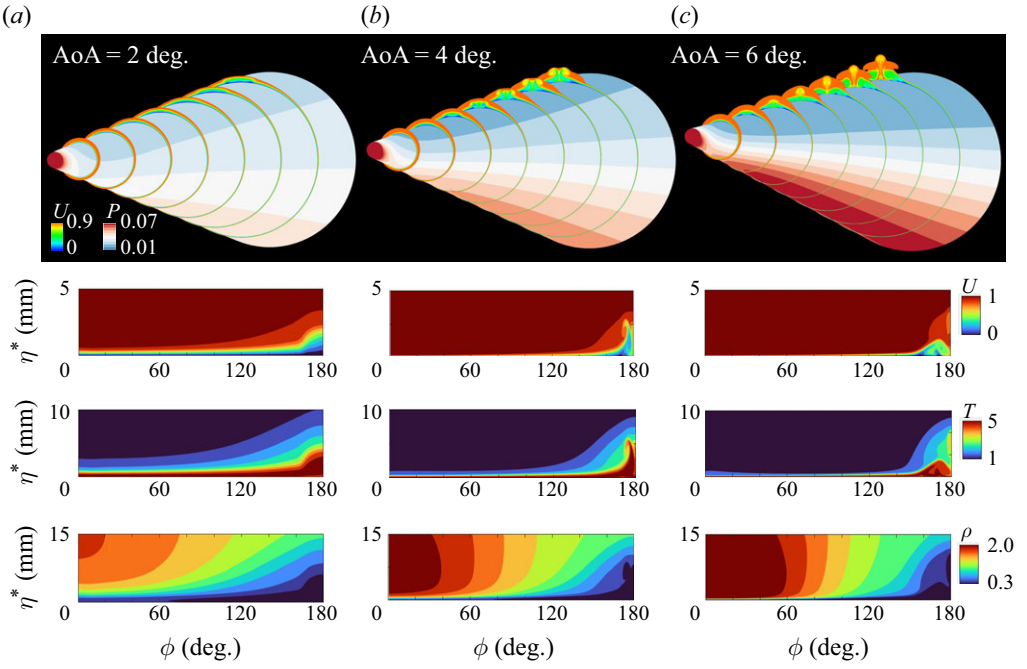


Figure 2. Base-flow characteristics for three cases with different AoA: (*a*) 2°, (*b*) 4° and (*c*) 6°. Top row: contours of the wall pressure and axial velocity at several axial locations from $X^* = 50$ to $X^* = 350$ mm. The last three rows display the axial velocity, temperature and density distribution, respectively, at $X^* = 250$ mm.

condition is used. The grid convergence has been tested by increasing the grid points along the azimuthal and wall-normal directions (see Appendix A).

The flow fields are illustrated by the surface pressure distribution and the axial velocity distribution at several cross-sections in figure 2. The distributions of the axial velocity, temperature and density at one representative station ($X^* = 250$ mm) are also displayed to highlight the azimuthal variations of the base flow. As expected, the azimuthal pressure gradient is present, driving the fluid towards the leeward region. Increasing the AoA strengthens the pressure gradient, leading to a more prominent vortical structure in the vicinity of the leeward ray.

2.3. *Governing equations of disturbances*

We concentrate on the linearised compressible Navier–Stokes equations describing the evolution of infinitesimal perturbations in a 3-D geometry with two rapidly varying (wall-normal and azimuthal) directions and one slowly varying (streamwise) direction. We decompose the flow state $\boldsymbol{Q} \equiv (\rho, u, v, w, T)^{tr}$ into the base flow $\bar{\boldsymbol{q}} \equiv (\bar{\rho}, \bar{u}, \bar{v}, \bar{w}, \bar{T})^{tr}$ plus the infinitesimal disturbances $\boldsymbol{q'} = (\rho', u', v', w', T')^{tr}$, where tr stands for the transpose and u, v, w denote the velocity components in the streamwise, wall-normal and azimuthal directions, respectively. We seek the optimal response to the inlet disturbance or the external forcing in the frequency domain, that is, considering a harmonic forcing at frequency ω, $\boldsymbol{f} = \hat{\boldsymbol{f}} e^{-i\omega t}$ and the corresponding response $\boldsymbol{q'} = \hat{\boldsymbol{q}} e^{-i\omega t}$. This problem can be readily formulated in an input–output framework:

$$\mathcal{P}\hat{\boldsymbol{q}} = \mathcal{C}\hat{\boldsymbol{f}}, \tag{2.6}$$

$$\hat{\boldsymbol{\psi}} = \mathcal{D}\hat{\boldsymbol{q}}, \tag{2.7}$$

https://doi.org/10.1017/jfm.2025.199 Published online by Cambridge University Press

where $\mathcal{P}$ is the HLNS operator; $\hat{\boldsymbol{f}}$ denotes the input; $\hat{\psi}$ designates the output; and $\mathcal{C}$ and $\mathcal{D}$ are projectors (i.e. $\mathcal{C}\mathcal{C}=\mathcal{C}$, $\mathcal{D}\mathcal{D}=\mathcal{D}$) specifying how the input enters into the state equation and how the output extracts from the state $\hat{\boldsymbol{q}}$. We define, respectively, the inner product and the energy-weight inner product:

$$(\hat{\boldsymbol{q}},\hat{\boldsymbol{q}})\equiv\int\hat{\boldsymbol{q}}^{\dagger}\hat{\boldsymbol{q}}\mathrm{d}\Omega,\quad(\hat{\boldsymbol{q}},\hat{\boldsymbol{q}})_E\equiv\int\hat{\boldsymbol{q}}^{\dagger}\boldsymbol{M}\hat{\boldsymbol{q}}\mathrm{d}\Omega,\quad(\hat{\boldsymbol{f}},\hat{\boldsymbol{f}})_F\equiv\int\hat{\boldsymbol{f}}^{\dagger}\boldsymbol{Q}\hat{\boldsymbol{f}}\mathrm{d}\Omega,\tag{2.8}$$

where

$$\boldsymbol{M}\equiv\mathrm{diag}\left(\frac{\bar{T}}{\bar{\rho}\gamma M_{\infty}^2},\bar{\rho},\bar{\rho},\bar{\rho},\frac{\bar{\rho}}{\gamma(\gamma-1)M_{\infty}^2\bar{T}}\right)\tag{2.9}$$

represents the response (Chu's) energy weight (Chu 1965), $\boldsymbol{Q}$ the forcing energy weight that will be defined later, Ω the domain where the shape function resides and $\dagger$ the transpose conjugate quantities. The input and output can be related by the transfer (resolvent) operator $\mathcal{H}$ as

$$\hat{\boldsymbol{\psi}}=\mathcal{D}\mathcal{P}^{-1}\mathcal{C}\hat{\boldsymbol{f}}\equiv\mathcal{H}\hat{\boldsymbol{f}}.\tag{2.10}$$

2.4. *Eigenspectrum, pseudospectrum and local optimal growth analyses*

When discarding the forcing term and adopting the parallel-flow assumption (i.e. $\partial\bar{\boldsymbol{q}}/\partial\xi=0$), we can introduce the ansatz $\hat{\boldsymbol{q}}=\check{\boldsymbol{q}}\mathrm{e}^{i\alpha\xi}$ into (2.6) and obtain the 2-D nonlinear eigenvalue problem:

$$\mathcal{P}\hat{\boldsymbol{q}}\equiv\check{\mathcal{P}}(\alpha)\check{\boldsymbol{q}}=0.\tag{2.11}$$

The real and imaginary parts of an eigenvalue α represent the wavenumber and growth rate of the associated eigenmode. Equation (2.11) can be rewritten as a numerically tractable linear eigenvalue problem:

$$\begin{pmatrix}\boldsymbol{0}&\mathcal{I}\\-\mathcal{A}_0&-\mathcal{A}_1\end{pmatrix}\begin{pmatrix}\check{\boldsymbol{q}}\\\alpha\check{\boldsymbol{q}}\end{pmatrix}=\alpha\begin{pmatrix}\mathcal{I}&\boldsymbol{0}\\\boldsymbol{0}&\mathcal{A}_2\end{pmatrix}\begin{pmatrix}\check{\boldsymbol{q}}\\\alpha\check{\boldsymbol{q}}\end{pmatrix},\tag{2.12}$$

or in a compact form:

$$\boldsymbol{A}_f\boldsymbol{q}=\alpha\boldsymbol{B}_f\boldsymbol{q}.\tag{2.13}$$

Here, $\mathcal{A}_0$, $\mathcal{A}_1$, $\mathcal{A}_2$ are linear operators for which the representations are give in Chen *et al.* (2022) and $\mathcal{I}$ is the identity operator; $\boldsymbol{A}_f\equiv[\boldsymbol{0},\mathcal{I};-\mathcal{A}_0,-\mathcal{A}_1]$, $\boldsymbol{B}_f\equiv[\mathcal{I},\boldsymbol{0};\boldsymbol{0},\mathcal{A}_2]$ and $\boldsymbol{q}\equiv[\check{\boldsymbol{q}};\alpha\check{\boldsymbol{q}}]$.

As mentioned above, the crossflow modes are highly sensitive, which can be best illustrated by the pseudospectrum (Trefethen & Embree 2005). The pseudospectrum can be characterised by the resolvent norm as

$$\|(\alpha\boldsymbol{B}_f-\boldsymbol{A}_f)^{-1}\|>\epsilon^{-1},\tag{2.14}$$

which quantifies physically the maximum response of the flow to any forcing. When the operator is non-normal, the resolvent norm may retain extremely large values even far from the spectrum.

Since the problem is of high dimension, the computation of the resolvent norm is too expensive. In practice, we can consider a low-dimensional approximation (Reddy *et al.* 1993) as

$$\|(\alpha\boldsymbol{B}_f-\boldsymbol{A}_f)^{-1}\|\approx\|(\alpha\boldsymbol{\Psi}^{\dagger}\boldsymbol{B}_f\boldsymbol{\Psi}-\boldsymbol{\Psi}^{\dagger}\boldsymbol{A}_f\boldsymbol{\Psi})^{-1}\|,\tag{2.15}$$

https://doi.org/10.1017/jfm.2025.199 Published online by Cambridge University Press

where $\boldsymbol{\Psi}$ is a matrix whose columns form an orthonormal basis for the subspace spanned by a moderate number of eigenvectors of (2.12).

In the framework of the local optimal growth analysis (with the parallel-flow assumption), a disturbance at frequency ω is approximately represented by a linear combination of n eigenmodes:

$$\boldsymbol{q}'(t, \xi, \eta, \phi) = \exp(-i\omega t) \sum_{k=1}^{n} \kappa_k \breve{\boldsymbol{q}}_k(\eta, \phi) \exp(i\alpha_k \xi). \tag{2.16}$$

The vector-function $\breve{\boldsymbol{q}}_k$ corresponds to the kth eigenfunction. The coefficients κ_k are optimised to achieve the maximum energy growth at the specific downstream coordinate (Hanifi *et al.* 1996; Tumin & Reshotko 2001)

$$G = \max \frac{(\boldsymbol{q}'(\xi), \boldsymbol{q}'(\xi))_E}{(\boldsymbol{q}'_0, \boldsymbol{q}'_0)_E} = \| \boldsymbol{F} \boldsymbol{\Lambda}_\xi \boldsymbol{F}^{-1} \|_2^2, \tag{2.17}$$

where $(\boldsymbol{q}'_0, \boldsymbol{q}'_0)_E$ corresponds to the energy at the initial location,

$$\boldsymbol{\Lambda}_\xi = \mathrm{diag}(\exp(i\alpha_1 \xi), \exp(i\alpha_2 \xi), \ldots, \exp(i\alpha_n \xi)) \tag{2.18}$$

and the matrix $\boldsymbol{F}$ is defined with help of the matrix $\boldsymbol{\Theta}$:

$$\boldsymbol{F}^\dagger \boldsymbol{F} = \boldsymbol{\Theta}, \quad \Theta_{k,l} = (\breve{\boldsymbol{q}}_{\boldsymbol{k}}, \breve{\boldsymbol{q}}_{\boldsymbol{l}})_E. \tag{2.19}$$

The resulting maximum energy gain can be determined by using the singular value decomposition.

2.5. *Global optimality system with variational formulation*

We will proceed to derive the global optimality system which takes the streamwise variations of the base flow into account (i.e. without the parallel-flow assumption).

For global non-modal analysis in 3-D boundary layers, the matrix representation like (2.16)–(2.19) for $\mathcal{H}$ is generally unavailable, and the matrix-free method is preferred. Thus, it is customary to reformulate the optimal problem in a variational framework to facilitate calculation. The Lagrangian functional for this problem reads

$$J = (\mathcal{D}\hat{\boldsymbol{q}}, \mathcal{D}\hat{\boldsymbol{q}})_E - 2\mathrm{Re}(\hat{\boldsymbol{p}}, \mathcal{P}\hat{\boldsymbol{q}} - \mathcal{C}\hat{\boldsymbol{f}}) - \lambda \left((\mathcal{C}\hat{\boldsymbol{f}}, \mathcal{C}\hat{\boldsymbol{f}})_F - 1 \right), \tag{2.20}$$

where $\hat{\boldsymbol{p}}$, the Lagrange multiplier, is referred to as the adjoint variable; λ is another Lagrange multiplier implementing the restriction on the input magnitude; and $\mathrm{Re}(\cdot)$ is the real part.

At the stationary point of the Lagrangian functional, we have, aside from the state equation (2.6) and the input energy constraint $(\mathcal{C}\hat{\boldsymbol{f}}, \mathcal{C}\hat{\boldsymbol{f}})_F = 1$, the adjoint equation

$$\mathcal{P}^\dagger \hat{\boldsymbol{p}} = \boldsymbol{M}\mathcal{D}\hat{\boldsymbol{q}} \tag{2.21}$$

and the optimality condition

$$\mathcal{C}\hat{\boldsymbol{p}} = \lambda \boldsymbol{Q}\mathcal{C}\hat{\boldsymbol{f}}, \tag{2.22}$$

which implies that the optimal forcing should be aligned with the adjoint state. Here $\mathcal{P}^\dagger$ is the adjoint operator such that

$$(\hat{\boldsymbol{p}}, \mathcal{P}\hat{\boldsymbol{q}}) = (\mathcal{P}^\dagger \hat{\boldsymbol{p}}, \hat{\boldsymbol{q}}) \equiv (\tilde{\mathcal{P}}^\dagger \hat{\boldsymbol{p}}, \hat{\boldsymbol{q}}) + \int \nabla \cdot \Gamma(\hat{\boldsymbol{p}}, \hat{\boldsymbol{q}}) \mathrm{d}\Omega, \tag{2.23}$$

https://doi.org/10.1017/jfm.2025.199 Published online by Cambridge University Press

where Γ is known as the bilinear concomitant representing the boundary terms in the three directions and $\tilde{\mathcal{P}}^\dagger$ does not contain the boundary terms. Here, the boundary conditions of the adjoint variable are chosen such that the boundary terms vanish except for the streamwise boundary terms when considering the optimal inlet profiles. As such, the boundary-layer terms can be converted to a more convenient form as

$$\int \nabla \cdot \Gamma(\hat{\boldsymbol{p}}, \hat{\boldsymbol{q}}) \mathrm{d}\Omega = \int (\boldsymbol{B}^\dagger \hat{\boldsymbol{p}})^\dagger \{\delta(\xi - \xi_1) - \delta(\xi - \xi_0)\} \hat{\boldsymbol{q}} \mathrm{d}\Omega, \tag{2.24}$$

where $\delta(\xi)$ is the Dirac delta function defined as

$$\delta(\xi) = 0 \text{ for } \xi \neq 0 \text{ and } \int \delta(\xi) \mathrm{d}\xi = 1; \tag{2.25}$$

$\boldsymbol{B}$ denotes the coefficient operator/matrix pertaining to $\partial/\partial\xi$; and ξ_0, ξ_1 designates the inlet and outlet locations, respectively. Thus, the adjoint operator can be formally written as

$$\mathcal{P}^\dagger = \tilde{\mathcal{P}}^\dagger + \boldsymbol{B}^\dagger \{\delta(\xi - \xi_1) - \delta(\xi - \xi_0)\}. \tag{2.26}$$

Such definition of the adjoint operator helps put the optimal responses to inlet profiles and to external forcing into a uniform framework, and can be readily extended to incorporate other types of disturbances (e.g. blowing and suction).

Substituting (2.22) into (2.6) to eliminate the forcing term $\hat{\boldsymbol{f}}$, we obtain

$$\mathcal{P}\hat{\boldsymbol{q}} = \frac{1}{\lambda} \boldsymbol{Q}^{-1} \mathcal{C} \hat{\boldsymbol{p}}. \tag{2.27}$$

Equations (2.21) and (2.27) form an eigenvalue problem which can be written as a single eigenvalue equation:

$$\mathcal{P}^{\dagger^{-1}} \boldsymbol{M} \mathcal{D} \mathcal{P}^{-1} \boldsymbol{Q}^{-1} \mathcal{C} \hat{\boldsymbol{p}} = \lambda \hat{\boldsymbol{p}}, \tag{2.28}$$

where the leading eigenvalue λ is exactly the optimal gain to the optimal forcing, and can be readily obtained by iteratively solving the direct and adjoint equations up to a converged state.

2.5.1. *Type of forcing*

Two specific cases of $\mathcal{C}$ and $\mathcal{D}$ are considered in this paper. For the first case, we restrict the input as an impulse forcing at the inlet and the output as the state variables at the outlet such that the input and output behave like the Dirac delta function:

$$\mathcal{C} = \delta(\xi_0), \quad \mathcal{D} = \delta(\xi_1). \tag{2.29}$$

This case corresponds to the optimal response to the inlet perturbation. In this case, the forcing energy weight $\boldsymbol{Q} = \boldsymbol{M}$. In the second case, we prescribe $\mathcal{C} = \mathcal{D} = \boldsymbol{Q} = \mathcal{I}$ (the identity operator) to retrieve the classical input–output problem where the forcing and response are distributed in the entire domain.

For the optimal response to the inlet perturbation, we can derive an equivalent formulation that is more computationally tractable. Since $\mathcal{C}$, $\mathcal{D}$ satisfy (2.25), we can take the integral with respect to ξ in (2.6) such that the forcing only enters into the inlet profile of the state variable, $\hat{\boldsymbol{q}}_0$, and is null downstream.

As such, Lagrangian functional (2.30) can be reformulated as

$$J = (\hat{\boldsymbol{q}}_1, \hat{\boldsymbol{q}}_1)_{ES} - 2\mathrm{Re}(\hat{\boldsymbol{p}}, \mathcal{P}\hat{\boldsymbol{q}}) - \lambda \left((\hat{\boldsymbol{q}}_0, \hat{\boldsymbol{q}}_0)_{ES} - 1 \right), \tag{2.30}$$

https://doi.org/10.1017/jfm.2025.199 Published online by Cambridge University Press

where $\hat{\boldsymbol{q}}_1$ denotes the state profile at the outlet and $()_{ES}$ the energy-weight inner product over either the inlet or outlet. At the stationary point of J, we have the direct and adjoint equations

$$\mathcal{P}\hat{\boldsymbol{q}} = 0, \quad \tilde{\mathcal{P}}^{\dagger}\hat{\boldsymbol{p}} = 0, \tag{2.31}$$

and the optimality condition

$$\boldsymbol{B}^{\dagger}\hat{\boldsymbol{p}}_1 = -\boldsymbol{M}\hat{\boldsymbol{q}}_1, \quad \boldsymbol{B}^{\dagger}\hat{\boldsymbol{p}}_0 = \lambda\boldsymbol{M}\hat{\boldsymbol{q}}_0. \tag{2.32}$$

Again, the optimal growth can be readily obtained by iteratively solving the direct and adjoint equations with the optimality condition. The optimal N-factor quantifying the integrated growth rate of the optimal disturbance is then defined as

$$N = \frac{1}{2}\ln(\lambda). \tag{2.33}$$

In this work, we focus on the first type of forcing (i.e. the inlet–outlet optimal growth problem) and only give a brief discussion of the other one for the following considerations. Firstly, the inlet–outlet optimal growth problem has been extensively studied in other flow configurations, and is intimately connected to conventional modal analyses as well as experimental/simulation studies where disturbances are initiated at the inlet only. Therefore, comparison between the present study and those previous works can be easily made. Secondly, the integrated growth rate (N-factor) of the optimal disturbances, which is one of key ingredients in the transition prediction, is ill-defined when considering an unrestricted forcing as the inlet disturbance is prescribed null, but is well-defined for the inlet–outlet optimal growth problem. Thirdly, we find that the optimal disturbance evolution process and the pertaining growth mechanisms obtained from the non-modal analysis with unrestricted forcings are essentially the same as those from the inlet–outlet optimal growth analysis.

2.5.2. *Wavemaker*

One concept that we use in our subsequent analysis is that of structural sensitivity and the wavemaker (Giannetti & Luchini 2007). The wavemaker has its origin in global stability analysis and provides a way to highlight regions in which the global modes are most sensitive to flow-field changes (specifically, a localised flow feedback). Analogously, the resolvent wavemaker (Skene *et al.* 2022) suggests the regions where flow-field variations effectively change the optimal gain. The wavemaker Λ can be shown (as detailed in Appendix B) to take the form as

$$\Lambda \equiv \|\hat{\boldsymbol{q}}\|\|\hat{\boldsymbol{p}}\| = \lambda\|\hat{\boldsymbol{q}}\|\|\hat{\boldsymbol{f}}\|. \tag{2.34}$$

In this way, the wavemaker $\boldsymbol{\Lambda}(\xi, \eta, \phi)$ can be thought of as a field quantifying what changes to the optimal gain occur from localised feedback at each location.

2.6. *Parabolised stability equations*

At this point, no approximation has been made. Our intention is to find a set of linear governing equations that are parabolic in nature. Such a system can be solved efficiently by employing marching techniques, and allows for extensive parametric studies. To this end, we can take the PSE ansatz for the forcing (if being distributed over the entire domain) as well as the response since the base flow varies slowly in the streamwise direction:

$$\hat{\boldsymbol{f}}(\xi, \eta, \phi) = \tilde{\boldsymbol{f}}(\xi, \eta, \phi)\exp\left(i\int_{\xi_0}^{\xi}\tilde{\alpha}(s)\mathrm{d}s\right) + \text{c.c.} \tag{2.35}$$

https://doi.org/10.1017/jfm.2025.199 Published online by Cambridge University Press

and

$$\hat{\boldsymbol{q}}(\xi,\eta,\phi)=\tilde{\boldsymbol{q}}(\xi,\eta,\phi)\exp\left(i\int_{\xi_0}^{\xi}\tilde{\alpha}(s)\mathrm{d}s\right)+\text{c.c.},\tag{2.36}$$

where the wavenumber $\tilde{\alpha}(\xi)$ is real and c.c. designates the complex conjugate part. In order to make the exponential part absorb the streamwise oscillation of the disturbance as much as possible, the real streamwise-varying wavenumber is determined iteratively by

$$\tilde{\alpha}^{new}=\tilde{\alpha}^{old}+Im\left\{\frac{1}{E}\iint\tilde{\rho}^{\dagger}\frac{\partial\tilde{\rho}}{\partial\xi}\frac{\bar{T}}{\bar{\rho}\gamma M_{\infty}^{2}}+\bar{\rho}\left(\tilde{u}^{\dagger}\frac{\partial\tilde{u}}{\partial\xi}+\tilde{v}^{\dagger}\frac{\partial\tilde{v}}{\partial\xi}+\tilde{w}^{\dagger}\frac{\partial\tilde{w}}{\partial\xi}\right)+\frac{\bar{\rho}\tilde{T}^{\dagger}\partial\tilde{T}/\partial\xi}{\gamma(\gamma-1)M_{\infty}^{2}\bar{T}}\mathrm{d}\eta\,\mathrm{d}\phi\right\},\tag{2.37}$$

where E is the disturbance energy defined as (Chu 1965)

$$E=\iint\frac{\bar{T}}{\bar{\rho}\gamma M_{\infty}^{2}}|\tilde{\rho}|^{2}+\bar{\rho}(|\tilde{u}|^{2}+|\tilde{v}|^{2}+|\tilde{w}|^{2})+\frac{\bar{\rho}}{\gamma(\gamma-1)M_{\infty}^{2}\bar{T}}|\tilde{T}|^{2}\mathrm{d}\eta\mathrm{d}\phi.\tag{2.38}$$

Consequently, the second-order, viscous derivative terms of the amplitude function in ξ can be neglected. Introduction of the ansatz (2.36) in (2.6) yields the plane-marching parabolised stability equations (PSE3D):

$$\mathcal{P}_{PSE}\tilde{\boldsymbol{q}}\equiv\left(\boldsymbol{A}+\boldsymbol{B}\frac{\partial}{\partial\xi}\right)\tilde{\boldsymbol{q}}=\mathcal{C}\tilde{\boldsymbol{f}},\tag{2.39}$$

where $\mathcal{P}_{PSE}$ denotes the parabolised linearised Navier–Stokes operator.

Similarly, the PSE ansatz can also be introduced in the adjoint variables:

$$\hat{\boldsymbol{p}}(\xi,\eta,\phi)=\tilde{\boldsymbol{p}}(\xi,\eta,\phi)\exp\left(-i\int_{\xi_0}^{\xi}\tilde{\alpha}(s)\mathrm{d}s\right)+\text{c.c.}\tag{2.40}$$

As a result, the adjoint equation (2.21) is represented by the adjoint parabolised stability equations (APSE3D):

$$\mathcal{P}_{APSE}\tilde{\boldsymbol{p}}\equiv\left(\boldsymbol{A}^{\dagger}-\boldsymbol{B}^{\dagger}\frac{\partial}{\partial\xi}\right)\tilde{\boldsymbol{p}}=\boldsymbol{M}\mathcal{D}\tilde{\boldsymbol{q}}.\tag{2.41}$$

The wavenumber $\tilde{\alpha}$ of the APSE can be either determined by a similar normalisation to (2.37) or simply prescribed the same value of the PSE solution of the latest iteration as suggested by Dobrinsky (2002). Both normalisation strategies lead to almost identical results (not shown here). The representations for $\mathcal{P}_{PSE}$ and $\mathcal{P}_{APSE}$ are detailed in Appendices D and E.

It is well known that some streamwise ellipticity remains in the streamwise pressure gradient term $\partial\tilde{p}/\partial\xi$ and may cause numerical instability. To eliminate the residual ellipticity, the streamwise pressure gradient term is either dropped from the equations as justified in Tempelmann *et al.* (2010) and Paredes *et al.* (2019) for stationary disturbances or replaced by $\Omega_{PNS}\partial\tilde{p}/\partial\xi$ for non-stationary disturbances, where Ω_{PNS} is the Vigneron parameter (Vigneron *et al.* 1978) defined as

$$\Omega_{PNS}=\min\{1,\,M_{\infty}^{2}\bar{u}^{2}/\bar{T}\}.\tag{2.42}$$

As criticised by Towne *et al.* (2019), equation (2.37) constrains the disturbances to have a unique, local wavenumber at any streamwise location such that PSEs are likely to encounter difficulties when the perturbation field contains multiple modes with disparate

https://doi.org/10.1017/jfm.2025.199 Published online by Cambridge University Press

streamwise wavenumbers or wavelengths. Towne *et al.* (2019) have shown that the errors introduced by the regularisation techniques of PSEs are proportional to the differences of the wavenumbers (or equivalently the distance between modes in the spectrum). Nevertheless, our local optimal growth analysis results in § 3 indicate that the optimal growth perturbations primarily comprise modes concentrating in a small portion of the entire spectrum as is also observed by Hanifi *et al.* (1996). This is reasonable since disturbances with close wavenumbers or phase velocities could efficiently interfere to achieve the optimal non-modal growth. Therefore, the absolute differences of the wavenumbers of these significant modes and the errors pertaining to PSEs will be small. More detailed verifications and discussions can be found in Appendix C.

2.6.1. *Boundary conditions and grid system*

The boundary conditions for the adjoint variables ($\hat{\boldsymbol{p}} = (\hat{\rho}_p, \hat{u}_p, \hat{v}_p, \hat{w}_p, \hat{T}_p)^{tr}$) are chosen so that the irrelevant boundary terms arising from the integration by parts vanish. At the wall, we have

$$\hat{u} = \hat{v} = \hat{w} = \hat{T} = 0, \quad \hat{\rho}_p = \hat{u}_p = \hat{v}_p = \hat{w}_p = \hat{T}_p = 0. \tag{2.43}$$

At the upper boundary, we set

$$\hat{u} = \hat{v} = \hat{w} = \hat{T} = 0, \quad \hat{u}_p = \hat{v}_p = \hat{w}_p = \hat{T}_p = 0. \tag{2.44}$$

Symmetry boundary conditions are implemented at the leeward and windward rays. Numerical tests indicate (not shown here) that using antisymmetric boundary conditions introduces negligible differences into low-frequency optimal disturbances but slightly underestimates the energy growths for high-frequency optimal disturbances. A fourth-order finite-difference scheme is used to discretise the azimuthal and wall-normal directions, while a second-order Euler backward scheme is applied in the streamwise direction. The grid resolution of 200×120 for the azimuthal and wall-normal directions is used for the cases with 2° and 4° AoA, while the azimuthal points are increased to 300 for the largest-AoA case. The solution was tested by changing the number of grid points and it was found to be grid-independent.

The initial guess contains the shape function/external forcing and the wavenumber. In the present study, two types of initial guesses have been used. For the first type, the initial value of the shape function/external forcing at every grid point is independently generated by the random function and is then normalised so that the initial disturbance/forcing energy is unity; the initial wavenumber is arbitrarily prescribed a moderate value (usually $\tilde{\alpha} \in (0, 1)$). Given the initial condition, the PSEs march forward until reaching the outlet station where the APSEs start to march backward. The initial condition is then updated based on the APSE results. Once converged, the optimal profiles/forcings serve as the second-type initial guess for the calculation in the nearby parameter space (e.g. slightly different frequencies, inlet/outlet stations). For either type of the initial guess, the PSE–APSE loop turns out to be robust and can reach converged results (relative difference in N-factors between two successive loops being smaller than 0.01) within 3 (for the second type) to 10 (for the first type) loops.

3. Results for the case of 2° AoA

In this section, we present results for the case of 2° AoA, scrutinising the salient features of the non-modal growth over a truly 3-D boundary layer. The results for the other AoA cases are briefly discussed in the next section.

https://doi.org/10.1017/jfm.2025.199 Published online by Cambridge University Press

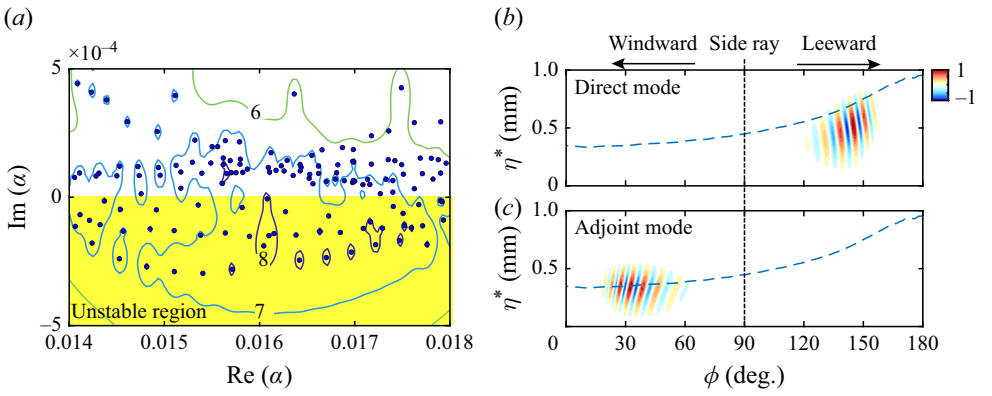


Figure 3. (*a*) Eigenspectrum (circles) and pseudospectrum (solid lines) of the linearised Navier–Stokes operator for a frequency of 20 kHz at $X^* = 100$ mm. The isolines represent pseudospectrum given by $\log_{10}\epsilon^{-1}$ contours, with ϵ ranging from 10^{-8} to 10^{-6}. The real parts of (*b*) the normalised $\hat{u}$ shape function for the mode $\alpha = 0.0172 - 0.0002i$ and (*c*) its adjoint. The boundary-layer edge (dashed line) is also displayed.

A representative pseudospectrum obtained from (2.14)–(2.15) for a frequency of 20 kHz at $X^* = 100$ mm is shown in figure 3(*a*). Many unstable modes can be observed, as expected, and they almost all lie within the contour line of $\|(\alpha \boldsymbol{B}_f - \boldsymbol{A}_f)^{-1}\| = 10^7$, meaning that one cannot exactly distinguish any of these unstable modes under perturbations as small as 10^{-7}. Such a high sensitivity of the eigenvalues obviously stems from the non-normality of the operator which can in turn cause a substantial transient growth.

The non-normality of the operator can be further inferred by inspecting figure 3(*b*, *c*), showing the spatial distribution of a typical direct–adjoint mode pair. The boundary-layer edge ($y_{BLe}(\phi)$) throughout this paper is defined as the location for which the local total enthalpy equals 99 % of the free-stream total enthalpy (h_e):

$$\left| \frac{h(y_{BLe}(\phi))}{h_e} - 0.99 \right| < 0.01. \tag{3.1}$$

The total enthalpy is given as

$$h \equiv \frac{\bar{T}}{(\gamma - 1)M_\infty^2} + \frac{1}{2}(\bar{u}^2 + \bar{v}^2 + \bar{w}^2). \tag{3.2}$$

The direct mode manifests as a tilted wavepacket structure lying on the leeward region, whereas the adjoint mode leaning in the opposite direction resides on the windward side. Such a clear separation in space between direct and adjoint modes indicates high sensitivities of the eigenvalues and a strong azimuthal non-normality induced by crossflow (Chomaz 2005).

3.1. *Optimal response to inlet perturbation*

As a first step we perform a parametric study on the optimal growth regarding the inlet/outlet positions (i.e. the projectors take the form of (2.29)) and the disturbance frequency. The results are displayed in figure 4 from which we can make several observations. First, the optimal disturbances undergo two distinct evolution stages: they initially experience a short-term, yet substantial transient growth (achieving growth of $\delta N \approx 4$ within about 20 mm) (stage I) followed by a relatively long-term moderate growth (stage II). The disturbance frequency seemingly affects the second stage only. The most

https://doi.org/10.1017/jfm.2025.199 Published online by Cambridge University Press

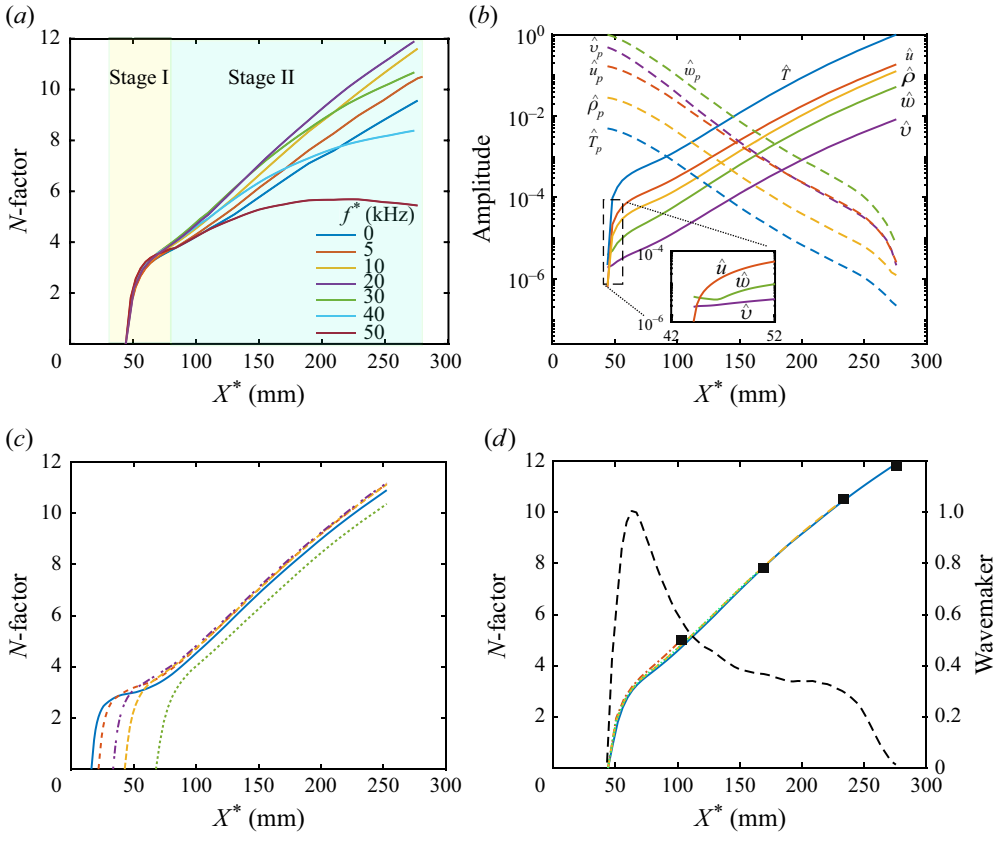


Figure 4. Parametric effects on the N-factors of the optimal growth: (a) different frequencies with $X_0^* = 44$ mm and $X_1^* = 275$ mm (note that the stationary one is approximated by results at a frequency of 0.01 kHz). (b) Streamwise evolution of the component amplitude of the direct (solid lines) and adjoint (dashed lines) states for a frequency of 20 kHz. (c) Different inlet locations with a fixed outlet location ($X_1^* = 250$ mm) and a frequency of 20 kHz. (d) Different outlet locations (marked by the square symbols) with a fixed inlet location ($X_0^* = 44$ mm) and a frequency of 20 kHz, along with the normalised wavemaker distribution ($\max_{\eta,\phi} \Lambda(\xi, \eta, \phi)$, dashed line).

amplified frequency is around 20 kHz whose amplitude evolutions of the direct and adjoint variables are shown in figure 4(b). It can be seen that the temperature fluctuation amplitude rapidly grows and soon becomes dominant, followed by the streamwise velocity component ($\hat{u}$). In contrast, the adjoint variables exhibit an opposite trend, suggesting a strong receptivity of the response to streamwise vortices ($\hat{v}$, $\hat{w}$) in the vicinity of the inlet. Second, there exists an optimal initial position given a frequency and an outlet position where the seeded disturbance can amplify maximally. For a frequency of 20 kHz, the optimal inlet location is at around $X^* = 40$ mm. At last, extending the outlet position with a given initial position does not modify the path but only raises the final energy gain reached by the disturbance. This can be explained by the wavemaker position. By definition (B12), the wavemaker should lie in the overlap region of the direct and adjoint states. Since the adjoint variable amplitude decays at a smaller rate in the vicinity of the inlet than the growth rate of the direct mode near the outlet, the wavemaker concentrates in a small region downstream of the inlet. Therefore, the optimal disturbance characteristics would be substantially preserved as long as the instability core (wavemaker) is included inside the spatial interval.

https://doi.org/10.1017/jfm.2025.199 Published online by Cambridge University Press

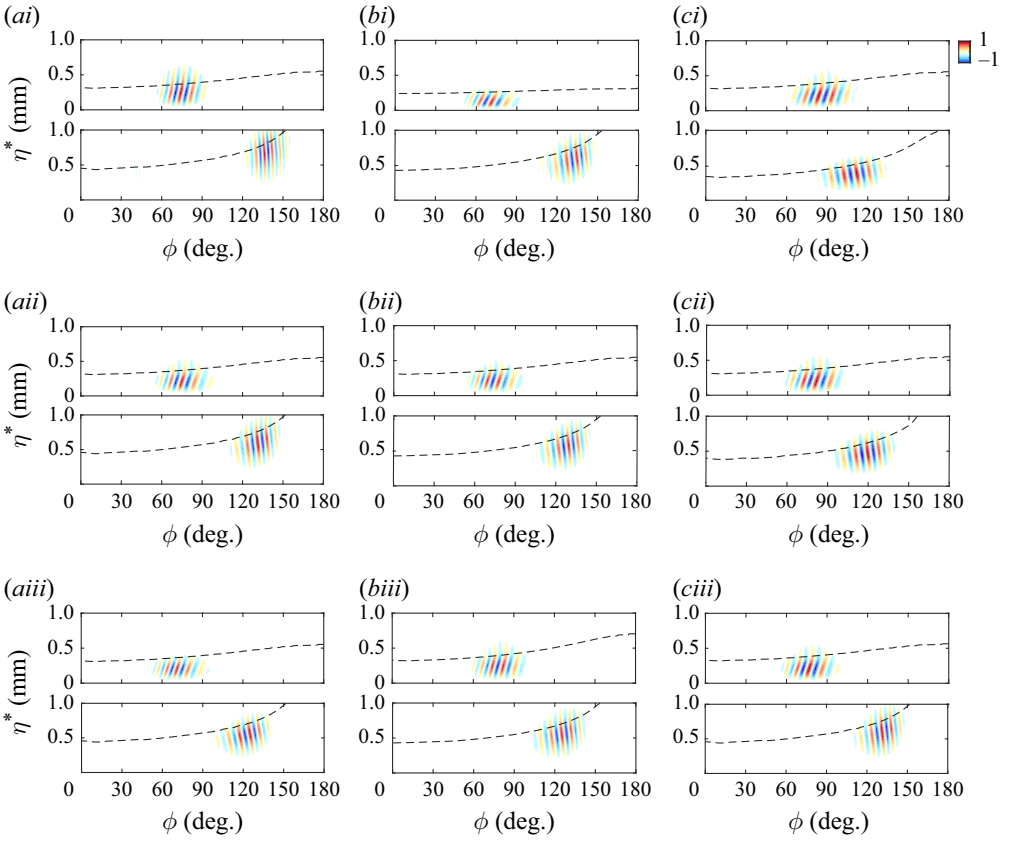


Figure 5. Parametric effects on the optimal disturbance profiles depicted by the real part of the temperature component at the inlet and outlet positions (shown in the upper and lower row, respectively, within each subplot). (*a*) Varying frequency for a fixed spatial domain (same as in figure 4*a*): (*ai*) stationary disturbance, (*aii*) 20 kHz, (*aiii*) 40 kHz. (*b*) Varying inlet positions for a given frequency (20 kHz) and a fixed outlet position ($X_1^* = 250$ mm): (*bi*) $X_0^* = 16$ mm, (*bii*) $X_0^* = 43$ mm, (*biii*) $X_0^* = 68$ mm. (*c*) Varying outlet positions for a given frequency (20 kHz) and a fixed inlet position ($X_0^* = 44$ mm): (*ci*) $X_1^* = 103$ mm, (*cii*) $X_1^* = 234$ mm, (*ciii*) $X_1^* = 275$ mm. The dashed line denotes the boundary-layer edge.

The parametric effects on the optimal disturbance profiles at the inlet and outlet locations are illustrated in figure 5. One can observe that the optimal disturbances all initially manifest as a tilted wavepacket lying preferentially on the windward side, very reminiscent of the shape function of a typical adjoint mode as displayed in figure 3. At the outlet position, they all tilt in the opposite direction and reside on the leeward side like a crossflow mode. This observation highlights the spatial separation between the highest-receptivity region (windward) and the highest-response region (leeward) for the optimal disturbances. With increasing disturbance frequency, the wavepacket is initially more tilted and ultimately resides closer to the side ray ($\phi = 90°$). On the other hand, the initial wavepacket progressively approaches the windward ray for a more upstream inlet, yet appears to be insensitive to the outlet location. This observation is important because one could obtain the optimal initial profile for even the entire model through performing optimal calculation over a relatively small domain where the wavemaker is strong.

Figure 6 shows the spatial structures of direct and adjoint states for three frequencies. We observe that the direct disturbance starts on the windward side and moves towards the leeward side, exhibiting a wedge-like amplitude envelope embodying several bent streaks

https://doi.org/10.1017/jfm.2025.199 Published online by Cambridge University Press

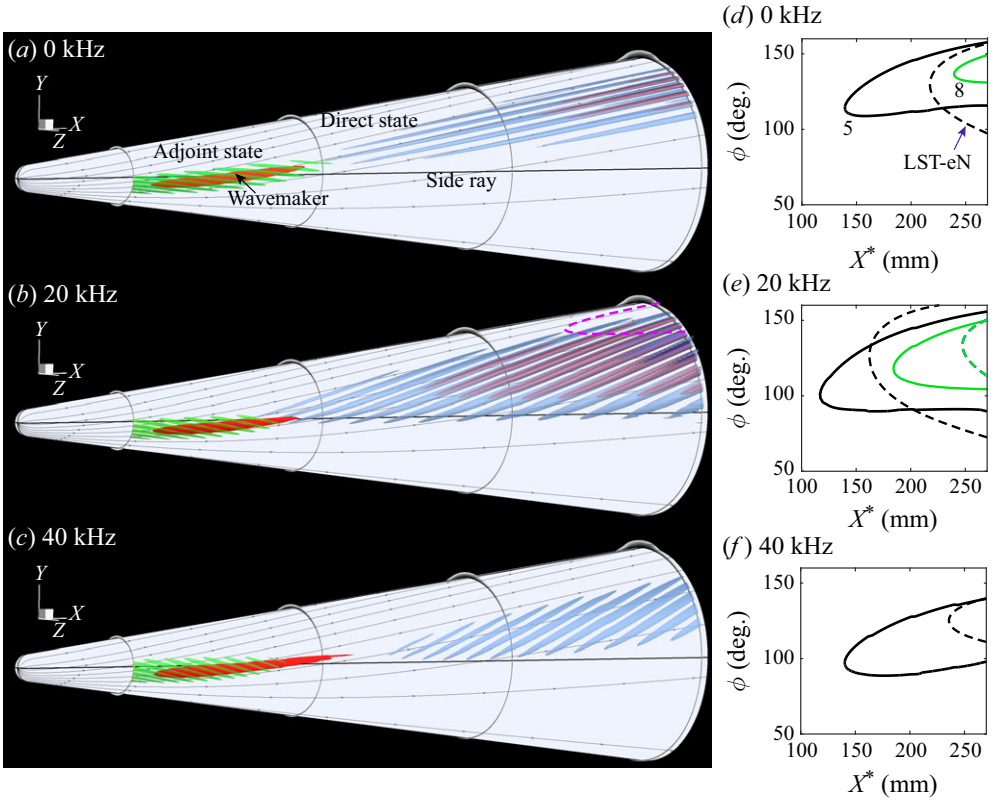


Figure 6. Spatial structures of the optimal disturbances of three representative frequencies, visualised by the isosurfaces of the real part of the temperature shape function with amplitude envelopes corresponding to $N_T =$ 5 (blue), $N_T = 8$ (red) and $N_T = 11$ (purple). The temperature shape function is normalised by the maximum value at the inlet position. Frequency (a) $f^* = 0$ kHz, (b) $f^* = 20$ kHz and (c) $f^* = 40$ kHz. Streamwise velocity distribution at four equal-distance streamwise slices (η–ϕ plane) starting from $X^* = 44$ mm to $X^* =$ 275 mm is also shown. The dashed pink line in (b) denotes the disturbance amplitude envelope corresponding to $N_T = 2.3$ obtained from PSE3D initiated by modal disturbances at 20 kHz. The spatial structures of the adjoint state (green, real $(\hat{T}_p) = 0.1|\hat{T}_p|_{max}$), the wavemaker (red, $0.5|\Lambda|_{max}$) and the edge streamlines are also displayed. $(d-f)$ The corresponding N-factor isolines (black: $N_{Chu} = 5$ and green: $N_{Chu} = 8$) based on the Chu energy in the X^*–ϕ plane, along with the LST-eN results (dashed lines).

inside; with increasing frequency, the core part of the spatial structure moves progressively towards the windward side, and the streaks are more prominently tilted. By contrast, the adjoint fluctuation, quantifying the high-receptivity region, lies preferentially on the windward side close to the inlet, exhibiting wave angles with respect to the streamwise direction opposite to those of the direct disturbances. Such remarkable spatial separation of the direct and adjoint states is indicative of the streamwise as well as azimuthal non-normality (Chomaz 2005). Interestingly, the wavemaker marking the structural sensitivity region manifests as a longitudinal structure slightly downstream from the inlet on the windward side, irrespective of the frequency. Consequently, one may expect to employ some control strategy in the wavemaker region for the crossflow instabilities with any frequency.

The area occupied by the amplitude envelope is obviously proportional to the N-factor of the disturbance. By analogy to the classical eN method utilising the 1-D stability analysis (LST), we define the local N-factor distribution on the cone surface based on the temperature disturbance amplitude as (see also Zhang *et al.* 2025)

https://doi.org/10.1017/jfm.2025.199 Published online by Cambridge University Press

$$N_T(\xi, \phi) = \ln(\max_{\eta} |\hat{T}(\xi, \eta, \phi)| / \max_{\eta,\phi} |\hat{T}(\xi_0, \eta, \phi)|). \tag{3.3}$$

Note that a similar formulation was adopted by Araya *et al.* (2023) with wall pressure as the alternative measure of disturbance amplitude. As such, the amplitude envelope of the optimal disturbance provides an upper bound of the transition front pertaining to a given N-factor in the eN framework. Alternatively, the local N-factor distribution can be depicted by the wall-normal integrated Chu energy as

$$N_{Chu}(\xi, \phi) = \ln\left(\int_0^{\eta_{max}} \hat{\boldsymbol{q}}^{\dagger} \boldsymbol{M} \hat{\boldsymbol{q}} \mathrm{d}\eta / E_0\right), \tag{3.4}$$

where E_0 as a normalisation factor denotes the maximum of the numerator at the inlet location. Quantitatively, N_T is slightly larger than N_{Chu} by a nearly constant value (about 1) for the present case. Figure 6($d-f$) compares the transition fronts corresponding to $N_{Chu} = 5$ and 8 (as long as the targeted N_{Chu} can be reached) predicted by the non-modal analysis and by 1-D modal analysis based on LST (LST-eN). The amplitude envelope obtained by PSE3D for the 20 kHz modal instability (pink dashed line) is also displayed in figure 6(b) for comparison. The first N-factor ($N_{Chu} = 5$) is typically associated with laminar–turbulent transition of stationary crossflow vortices in the incompressible regime (Bippes 1999), while the second ($N_{Chu} = 8$) is close to the transition N-factor of travelling crossflow waves on the Mach 6 HyTRV model (Chen *et al.* 2022). Evidently, the optimal disturbance amplitude envelopes significantly extend in the upstream direction the LST-eN envelope at the same N-factor as well as the modal PSE3D-eN envelope even with a much smaller N-factor ($N_T = 2.3$), highlighting the appreciable non-modal growth. Nevertheless, modal analyses also predict the predominance of the 20 kHz waves, suggesting that non-modal growth does not change the peak frequency. Another interesting observation is that the core part of the downstream optimal structure matches well with the most unstable region predicted by the LST-eN method, but is remarkably far away from the leeward ray compared with the 2-D modal amplitude envelope (pink dashed line). This implies that the optimal disturbance does exploit the crossflow instability, yet not in the same manner as a 2-D local crossflow mode does, which is discussed in detail later.

3.1.1. *Growth mechanism*

Figure 7 clearly illustrates how the optimal profile initiates a crossflow-instability wavepacket, from which an important insight into the physical mechanisms in stage I can be gained. Initially, the optimal profile gives rise to immediately downstream alternating positive and negative longitudinal vortical rolls with axes aligned along the axial direction, which are well known in shear-layer flows to be able to optimally leverage the lift-up effects. The lift-up effect can also be inferred from the observation that the initially dominant vortex components ($\hat{v}$, $\hat{w}$) are soon taken over by the streak component ($\hat{u}$) in amplitude, as displayed in figure 4(b). The initially strong vortex components are directly driven by the adjoint components ($\hat{v}_p$, $\hat{w}_p$). Despite weakening rapidly due to viscous dissipation, these longitudinal vortices induce counter-rotating vortices below, forming two-cell vorticity structures with axes being tilted with respect to the axial direction. Such vorticity structures are no longer optimal in the sense of the lift-up effect because of the counteracting forces from two opposite-orientation vorticity layers, yet are typical of crossflow instabilities (Wassermann & Kloker 2003) of which they can take advantage to sustain the downstream growth.

At the same time, the apparent change of the vorticity inclination in the cross-section as shown in figure 7(b–g) is indicative of the Orr mechanism that can enhance the lift-up effect as well as the near-wall vorticity induction by strengthening the primary vorticity.

https://doi.org/10.1017/jfm.2025.199 Published online by Cambridge University Press

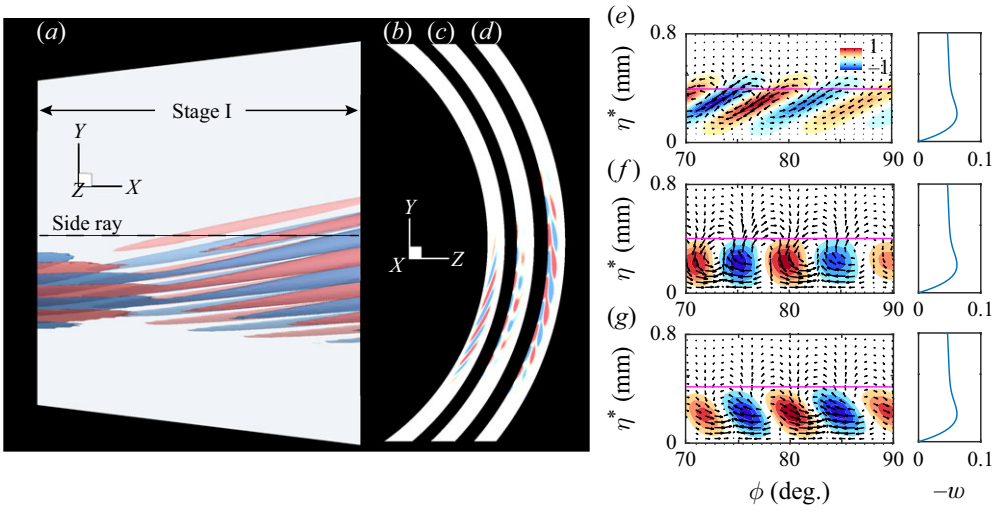


Figure 7. Optimal structure evolution in the first stage (44 mm $< X^* <$ 64 mm) depicted by (*a*) the isosurfaces of the streamwise vorticities (red: positive; blue: negative) and the axial vorticity distribution on the cross-sections at three successive axial stations: (*b*) $X^* = 44$ mm, (*c*) $X^* = 54$ mm and (*d*) $X^* = 64$ mm. The cross-section coordinates (Y, Z) have been enlarged twofold for facilitating comparison. (*e*–*g*) The corresponding streamwise velocity disturbance profiles at these three axial stations overlayed with the vector plot comprising the wall-normal and crossflow components. The pink line denotes the boundary-layer edge. The rightmost column shows the mean crossflow components at the peak location of the optimal disturbance.

By analogy to the analysis of Butler & Farrell (1992), the Orr mechanism in the present case is rooted in the production term, $-\mathrm{Re}(\hat{w}^{\dagger}\hat{v})(\partial\bar{w}/\partial\eta)$, stemming from the azimuthal momentum equation as is discussed later. When this term is positive, or equivalently the disturbance structure is tilted against the shear of the crossflow, the disturbance is able to gain energy from the mean flow. Otherwise, the disturbance would lose energy. Figure 7(*e*–*g*) reveals that the crossflow profile exhibits two distinct regions across the boundary layer with opposite sign pertaining to the shear term $(\partial\bar{w}/\partial\eta)$. As a result, if the disturbance gains energy in the upper region, it would return energy back to the base flow in the lower region with the same tilted direction. At the initial position, the disturbance structure well extends into the free stream and is tilted against the upper shear, favouring energy gain. The slanted structure soon turns upright at the next station and tilts along the opposite direction further downstream. Beyond the second station, the disturbances penetrate more deeply into the boundary layer, occupying almost equally the two shear regions of the crossflow, and the total energy transfer pertaining to the Orr mechanism should thus be smaller thereafter.

This vortex evolution process is representative of optimal disturbances, the quantitative difference being that the inclined angle of the two-cell vorticity structures increases with the frequency. As per the observations made so far, we might thus conclude that the non-modal growth of the optimal disturbance in stage I primarily stems from a synergistic combination of the lift-up effect and the Orr mechanism, which conforms with the optimal growth results for the infinite swept wing boundary layer (SWBL) (Tempelmann *et al.* 2010, 2012).

In the following, we consider whether the crossflow-instability wavepacket initiated by the optimal profile is governed by a dominating unstable mode as in the SWBL (Tempelmann *et al.* 2010). Figure 8(*a*) compares the N-factor of the optimal disturbance of 20 kHz and those calculated by PSE3D with initial profiles provided by different crossflow

https://doi.org/10.1017/jfm.2025.199 Published online by Cambridge University Press

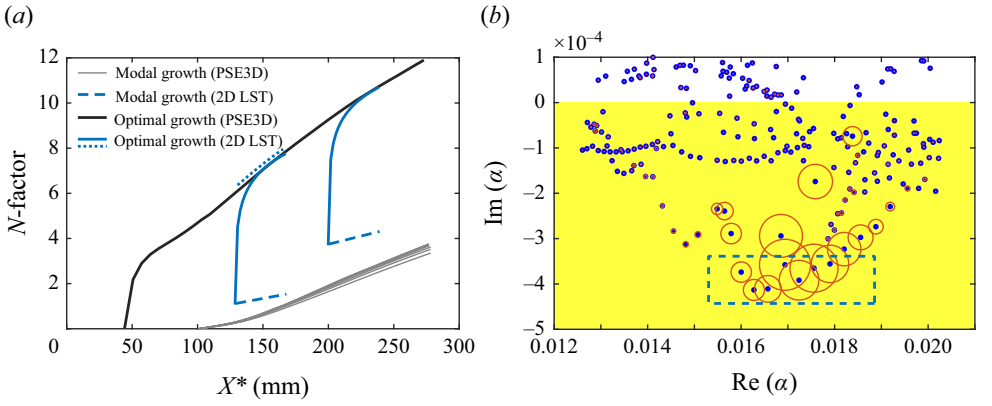


Figure 8. (*a*) Comparison of N-factor of the optimal disturbance at a frequency of 20 kHz and the crossflow modal disturbances obtained from PSE3D initiated by different crossflow modes at $X^* = 100$ mm at the same frequency (grey lines). The results from the local transient growth analysis (solid blue lines) and the most unstable mode obtained by 2-D LST (dashed blue lines) for two representative stations ($X^* = 134$ and 200 mm) are displayed, with an upward shift to facilitate the comparison. (*b*) Contributions of individual 2-D local modes to the local optimal growth at $X^* = 134$ mm, visualised by the circles sized proportional to the corresponding expansion coefficients κ_k. The energy gain of the disturbance superimposed by a few most unstable modes (delimited by the dashed box) is also shown in (*a*) (dotted blue line).

modes (see figure 3*a* for spectrum) at $X^* = 100$ mm (deemed close to the neutral location). Obviously, the optimal disturbance at stage II amplifies at a substantially larger rate than the modal disturbances do, indicating that it could not be well represented by a single mode. This is not surprising because the 2-D local crossflow instability spectrum as shown in figure 8(*b*) contains multiple unstable modes without a predominant one, in stark contrast to the SWBL case where generally only one unstable crossflow mode exists given a frequency and a wavenumber. The (linear) non-modal combinations among these similar-looking modes may yield a much more rapid energy growth than the most unstable mode, which could have been exploited by the optimal disturbance. To justify such speculation, we have conducted a local optimal growth analysis, (2.16)–(2.19), seeking an optimal combination of modes that yields the maximum energy growth at the specific distance downstream, for two representative stations.

The spectrum used in calculating the local optimal energy gain for $X^* = 134$ mm is displayed in figure 8(*b*). It contains a total of 208 modes, but only a small portion of the spectrum primarily comprising significantly unstable modes plays an important role. The corresponding optimal energy gain, shown in figure 8(*a*), clearly reveals the initial algebraic growth stage and the ensuing quasi-exponential growth stage. Here, the local optimal N-factor curves have been shifted in the vertical direction so that they are tangent to the global optimal N-factor curves. It should be noted that the local optimal growth analysis fails to capture initial energy gain due to the Orr and lift-up mechanisms (see Liu *et al.* (2024) for more details) which might need much more modes than presently used (Bagheri *et al.* 2009). Nevertheless, the growth rate pertaining to the quasi-exponential growth stage is substantially larger than that of the most unstable mode, and bears a striking resemblance to that of the global optimal disturbance for an appreciably long distance. The optimal energy gain based on a few most unstable modes (delimited by the dashed box) exhibits a diminishing algebraic growth, yet quantitatively the same exponential growth as the fuller spectrum. This indicates that the quasi-exponential growth stage is governed by the few most unstable modes while the less unstable modes would affect the initial algebraic growth stage only. Such observations seem to hold at other

https://doi.org/10.1017/jfm.2025.199 Published online by Cambridge University Press

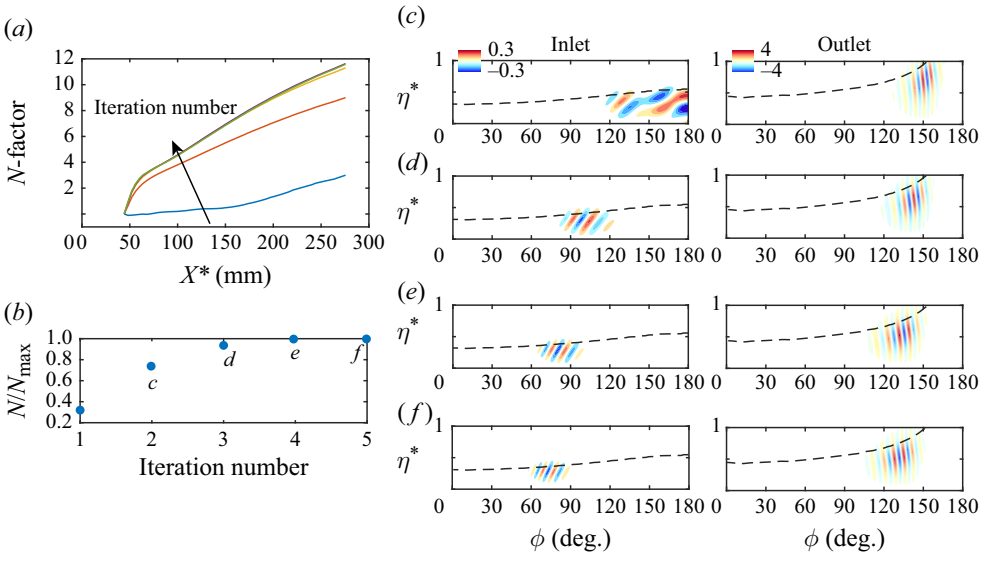


Figure 9. Convergence process of the optimal disturbance at 20 kHz in the streamwise range of (44, 275) mm initiated by a random profile: (*a*) the N-factor evolution, (*b*) the ratio of the outlet N-factor to the optimal one and (*c*–*f*) streamwise velocity profiles at the inlet and outlet for the second iteration to the fifth iteration, normalised by the cross-velocity components ($\sqrt{\hat{v}^2 + \hat{w}^2}$) with the dashed line denoting the boundary-layer edge.

stations as well, justifying the speculation that the optimal disturbance may have exploited the non-modal combination among the few most unstable modes locally to achieve the global optimal growth. Indeed, the global transient analysis on 2-D flow configurations has shown that superposition of non-normal global (even decay) modes recovers the convective (exponential) instability (Cossu & Chomaz 1997; Bagheri *et al.* 2009; Nichols & Lele 2011), during which the optimal disturbance is convected from upstream to downstream (Ehrenstein & Gallaire 2005; Alizard & Robinet 2007; Åkervik *et al.* 2008). Analogously, superposition of 2-D crossflow modes leads to an azimuthal shift of the disturbance structure from the windward side to the leeward side as the optimal disturbance travels downstream in the present 3-D configuration.

The above results reveal three active mechanisms beneath the optimal growth, i.e. the Orr mechanism, the lift-up effect and the crossflow instability mechanism manifesting in both the streamwise and azimuthal directions. A significant insight regarding the role played by these mechanisms can be gained from the typical convergence process of the optimal growth, as displayed in figure 9. We observe that after just one iteration the inlet disturbance structure already retrieves all the aforementioned mechanisms, yielding nearly 80 % of the final optimal energy gain (figure 9*b*): firstly, its streamwise velocity component is much smaller than the vortex component in amplitude, an indicator of the lift-up effect; secondly, the slanted structures in the η–ϕ plane suggest the Orr mechanism; finally, the outlet profile exhibiting typical crossflow-instability features implies the crossflow-instability mechanism. After one more iteration, the inlet disturbance structure entirely leans against the crossflow shear such that it can take full advantage of the Orr mechanism; moreover, the spatial separation is more pronounced, enhancing the disturbance energy gain along the azimuthal direction through crossflow instability. Further iteration drives the inlet disturbance to the windward side progressively, yet barely improves the optimal gain, indicating that the azimuthal crossflow-instability growth is

https://doi.org/10.1017/jfm.2025.199 Published online by Cambridge University Press

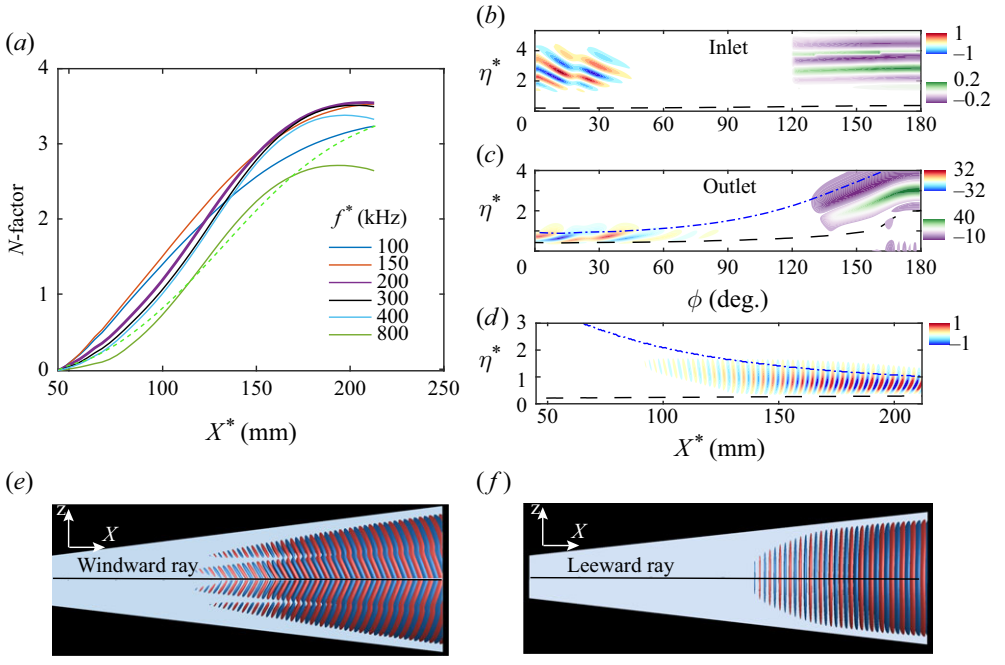


Figure 10. Results for optimal disturbances of high frequencies optimised over a streamwise interval corresponding to $x \in (44, 212)$ mm. (*a*) Evolution of N-factor of various frequencies. The dashed line denotes the result for 200 kHz optimised for the restricted azimuthal region $\phi \in (120°, 180°)$. (*b–d*) Contours of the normalised temperature of the optimal disturbance at 200 kHz displayed in the inlet (*b*) and outlet (*c*) as well as in the X–η plane at the windward ray ($\phi = 0°$). The temperature components at (*b*,*c*) are normalised by the total velocity amplitude, while those at (*d*) are normalised by the maximum temperature amplitude. The blue–red contours and the green–purple contours denote the optimal structure optimised for the entire azimuthal region and for the restricted azimuthal region, respectively. The dashed and dashed-dotted lines indicate the edge of the boundary layer, δ_h, and the edge of the entropy layer, δ_S, respectively. (*e*,*f*) Spatial structure evolution for the optimal disturbance at 200 kHz, optimised for the entire azimuthal region and for the restricted azimuthal region, respectively, depicted by the isosurfaces of the temperature disturbance (red: positive; blue: negative; amplitude corresponding to $N_T = 3.2$).

relatively weak compared to other mechanisms. In summary, the iteration process tends to first distil the lift-up effect and the streamwise crossflow instability mechanism, which can thus be viewed as most important for the optimal growth, and then fully exploits the Orr and azimuthal crossflow-instability mechanisms to achieve the maximum amplification.

3.1.2. *High-frequency optimal growth*

In addition to the low-frequency optimal disturbances, we also calculated optimal disturbances at high frequencies which exhibit totally different features from the former. Figure 10 depicts the evolution of N-factors of frequencies ranging from 100 to 800 kHz for a specified streamwise interval and the temperature contour of one representative frequency. One can observe moderate transient growths, albeit much weaker than the low-frequency optimal growth, experienced by a broadband disturbance far from the modal instability frequencies (around 1 MHz for Mack mode instabilities). The relative differences of the peak N-factors among various frequencies are less than 1, indicating a relatively flat frequency response. The optimal shape function, exemplified by the frequency of 200 kHz, concentrates in the domain between the boundary-layer edge and the entropy-layer edge of the windward side throughout the entire streamwise interval.

https://doi.org/10.1017/jfm.2025.199 Published online by Cambridge University Press

Following the work of Paredes *et al.* (2020), the entropy-layer edge, δ_S, is defined as the location where the local entropy increment is 0.25 times the entropy increment at the wall ($\Delta\bar{S}(\eta = \Delta_S) = 0.25\Delta\bar{S}_{wall}$). The entropy increment, $\Delta\bar{S}$, is defined with respect to the free-stream value, i.e. $\Delta\bar{S} = 1004\ln(\bar{T}) - 287\ln(\bar{P})$. The fact that the disturbance remains in the vicinity of the windward ray indicates that the aforementioned azimuthal shift of the low-frequency optimal disturbances is solely due to the crossflow instability, which is absent here. The mode shapes at the inlet and outlet positions exhibit opposite-slanted structures in both the azimuthal and streamwise directions, suggesting an Orr-like mechanism responsible for the transient growth. As opposed to the classical Orr mechanism which mainly amplifies the velocity components, the temperature component of the high-frequency perturbation is the prime benefactor (see figure 10*b*, *c*) from algebraic amplification where the temperature gradient within the entropy layer is a driving factor, as is shown later. Finally, the spatial evolution of the optimal disturbance at 200 kHz is illustrated in figure 10(*e*), featuring a wave-train structure in the vicinity of the windward ray with a preferential wave angle on either side.

It is noteworthy that Paredes *et al.* (2019) have also discovered entropy-layer travelling disturbances that experience appreciable non-modal growth on a hypersonic blunt cone at zero AoA. They (Paredes *et al.* 2020) later showed that a pair of oblique non-modal waves could induce onset of transition via oblique breakdown. Our work extends their results to a 3-D configuration, showcasing the optimal entropy-layer disturbances concentrating in the vicinity of the windward ray. Because the optimal disturbance on either side of the windward ray comprises exclusively components with wave angles of the same sign, prohibiting interactions between components with opposite wave angles, the classical oblique breakdown mechanism is not active here (see Chen *et al.* (2023) for detailed discussion). It is interesting to assess whether high-frequency disturbances can undergo transient growth in other places than the windward ray as well. A straightforward method is to calculate the optimal disturbance within a restricted azimuthal domain. As inferred from figure 10(*a,b,c,f*), the optimal disturbance restricted in the leeward region, exhibiting an essentially 2-D structure, turns out to enjoy a commensurate energy amplification as well through exploiting an Orr-like mechanism in the streamwise direction (not shown here).

3.2. *Optimal response to external forcing in the entire domain*

In this subsection, we present results for the optimal response to the external forcing in the entire domain. Without loss of generality, we set $\boldsymbol{Q} = \boldsymbol{I}$ in measuring the forcing energy. Because the inlet response is prescribed null for this case, the conventional N-factor would yield an infinitely large value. To circumvent such difficulty, we consider the integrated growth rate between the outlet and a position slightly downstream of the inlet. Figure 11 shows the results for a representative spatial interval $X^* \in (44, 215)$ mm. The N-factors starting from $X^* = 47$ mm in figure 11(*a*) feature an algebraic growth stage followed by a long-term (quasi-exponential growth) phase, and peak at 20 kHz, closely resembling the optimal growth results. Direct comparison between the dominant N-factor evolution for the optimal forcing case and the optimal inlet-profile case indicates that their differences lie primarily in the algebraic growth stage wherein the former is remarkably enhanced. Interestingly, the algebraic growth is more pronounced with increasing frequency, in stark contrast to the optimal inlet-profile case wherein it almost coincides for different frequencies.

The streamwise distribution of the component amplitude of the optimal forcing and the response for 20 kHz is displayed in figure 11(*b*). As expected, the forcing amplitudes exhibit an almost opposite trend against the response counterpart; they peak within the

https://doi.org/10.1017/jfm.2025.199 Published online by Cambridge University Press

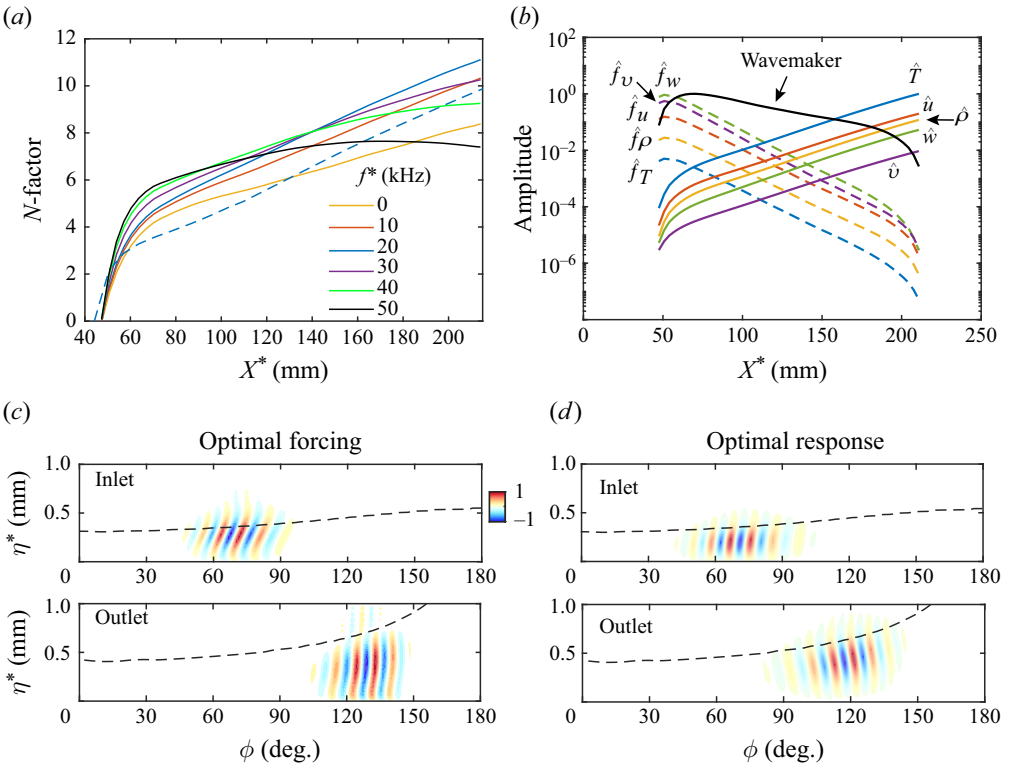


Figure 11. (*a*) The N-factor of the optimal response to external forcings at frequency ranging from $f^* = 0$ to $f^* = 50$ kHz, together with the optimal response to inlet profiles at 20 kHz (dashed line) for comparison. (*b*) Streamwise component amplitude evolution of the normalised optimal response (solid lines) and the normalised optimal forcing (dashed lines) for 20 kHz. The normalised resolvent wavemaker distribution ($\max_{\eta,\phi} \Lambda(\xi, \eta, \phi)$) is also displayed. The corresponding (*c*) optimal forcing and (*d*) response shape functions at the inlet (upper row) and outlet (lower row) positions, illustrated by $\hat{f}_u$ and $\hat{u}$.

algebraic growth stage and rapidly diminish downstream. Forcing terms on the ϕ- and η-direction momentum equations are dominant, implying that the optimal forcing tends to leverage the lift-up effect to prompt the energy growth by enhancing the streamwise vorticity. Moreover, the optimal forcing shape function shown in figure 11(*c*) is always tilted against the crossflow shear, suggesting that the optimal forcing exploits the Orr mechanism as well. The resulting response shown in figure 11(*d*) is very reminiscent of that in the optimal inlet-profile case. To conclude, the optimal disturbance under external forcing undergoes essentially the same evolution process with the same growth mechanisms as in the optimal inlet-profile case; the optimal forcing mainly acts on the algebraic growth stage (stage I) by constantly enhancing the lift-up and Orr mechanisms, yet barely affects the ensuing stage where the crossflow instability prevails.

As inferred from figures 12 and 6, the optimal forcing is exerted on the same position of the adjoint state except for the vicinity of the inlet where it manifests as longitudinal structures aligned with the axial direction. Since axially aligned vortices (with nearly zero streamwise wavenumber) are most favourable for the lift-up effect (Farrell & Ioannou 1993), the optimal forcing presumably takes more advantage from the lift-up effect, thus enhancing the algebraic growth. Moreover, the wavemaker almost coincides with that of the optimal inlet-outlet growth problem, implying the same localised feedback mechanisms for both cases.

https://doi.org/10.1017/jfm.2025.199 Published online by Cambridge University Press

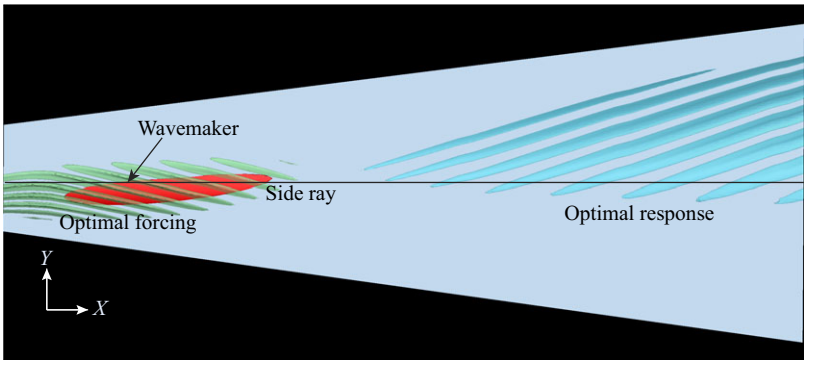


Figure 12. Spatial structure of the optimal forcing (green, $\mathrm{Re}(\hat{f}_T) = 10^{-5}$), the optimal response (blue, $\mathrm{Re}(\hat{T}) = 50\,000$) and the resolvent wavemaker (red, $0.5|\Lambda|_{max}$).

3.3. *Energy transfer analysis*

To further understand the energy growth mechanisms of the optimal disturbances, it is instructive to perform an energy transfer analysis. Following the work of Chen *et al.* (2017, 2023), the energy transfer under external forcings but without nonlinear interactions can be conveniently divided into four parts as

$$\frac{1}{E}\frac{\mathrm{D}}{\mathrm{D}t}E = \Pi + \Upsilon + \Xi + \Phi. \tag{3.5}$$

The production reads

$$\Pi = -\frac{1}{E}\mathrm{Real}\left[\iint \underbrace{\bar{\rho}\tilde{u}_i^{\dagger}\tilde{u}_j\frac{\partial \bar{u}_i}{\partial x_j}}_{\Pi^U_{u_iu_j}} + \underbrace{\frac{2\bar{\rho}}{\gamma(\gamma-1)M_\infty^2\bar{T}}\tilde{T}^{\dagger}\tilde{u}_i\frac{\partial \bar{T}}{\partial x_i}}_{\Pi^T_{u_i}} + \underbrace{\frac{2\bar{T}}{\gamma M_\infty^2\bar{\rho}}\tilde{\rho}^{\dagger}\tilde{u}_i\frac{\partial \bar{\rho}}{\partial x_i}}_{\Pi^\rho_{u_i}}\,\mathrm{d}\eta\,\mathrm{d}\phi\right], \tag{3.6}$$

$$(\tilde{u}_i)_{i=1,2,3} = (\tilde{u},\,\tilde{v},\,\tilde{w}), \quad (\bar{u}_i)_{i=1,2,3} = (\bar{u},\,\bar{v},\,\bar{w}), \quad (x_i)_{i=1,2,3} = (\xi,\,\eta,\,\phi), \tag{3.7}$$

representing the energy transfer from the mean flow to the disturbance. Note that the production contains three parts, i.e. the Reynolds stress work (Π^U), the energy transfer owing to the temperature gradient (Π^T) and the energy transfer owing to the density gradient (Π^ρ). The energy transfer directly driven by the external forcing, which vanishes in the inlet–outlet optimal growth problem, takes the form of

$$\Phi = \frac{1}{E}\mathrm{Real}\left[\iint \tilde{u}_i^{\dagger}\tilde{f}_{u_i} + \frac{2\bar{\rho}}{\gamma(\gamma-1)M_\infty^2\bar{T}}\tilde{T}^{\dagger}\tilde{f}_T + \frac{2\bar{T}}{\gamma M_\infty^2\bar{\rho}}\tilde{\rho}^{\dagger}\tilde{f}_d\mathrm{d}\eta\,\mathrm{d}\phi\right], \tag{3.8}$$

where $\tilde{f}_{u_i}$, $\tilde{f}_T$ and $\tilde{f}_d$ denote the forcing on the (three) momentum equations, the energy equation and the continuity equation, respectively. Here Υ is the energy transfer associated with the viscous and heat conduction terms and Ξ represents the remainder terms. Here we focus on the production terms and energy transfer pertaining to the external forcing only in an attempt to unveil the important driving factor during the energy growth of the optimal disturbances.

https://doi.org/10.1017/jfm.2025.199 Published online by Cambridge University Press

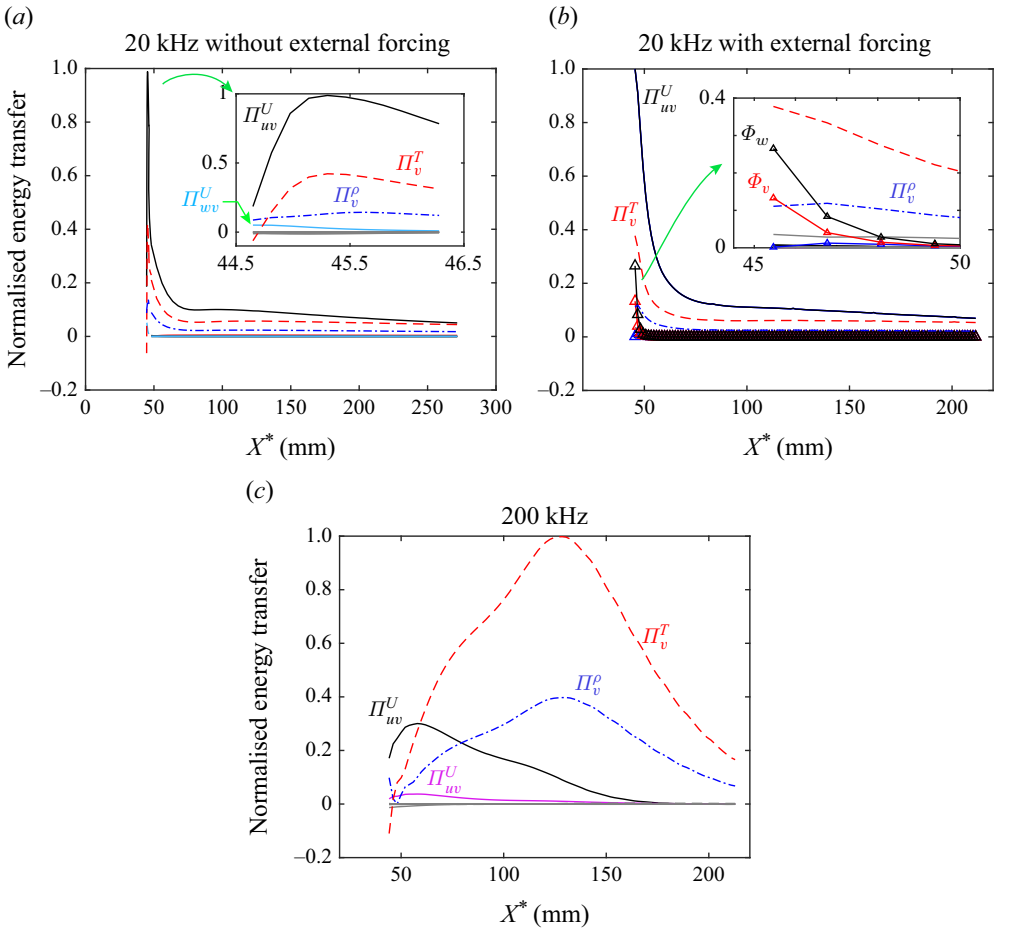


Figure 13. Streamwise evolution of the production terms normalised by the maximum value for the energy transfer of representative optimal disturbances: the low-frequency optimal disturbance at 20 kHz (with a zoom of the inlet) without (*a*) and with (*b*) distributed external forcing, and (*c*) the high-frequency optimal disturbance at 200 kHz without distributed forcing. Significant terms are labelled while others are plotted in grey.

Figure 13 displays the streamwise evolution of the normalised production terms for representative optimal disturbances. It can be seen that the three terms

$$\Pi^U_{uv} = -\frac{1}{E}\mathrm{Real}\left[\iint \bar{\rho}\tilde{u}^\dagger \tilde{v}\frac{\partial \bar{u}}{\partial \eta}\right], \quad \Pi^T_v = -\frac{1}{E}\mathrm{Real}\left[\frac{2\bar{\rho}}{\gamma(\gamma-1)M^2_\infty \bar{T}}\tilde{T}^\dagger \tilde{v}\frac{\partial \bar{T}}{\partial \eta}\right], \tag{3.9}$$

$$\Pi^\rho_v = -\frac{1}{E}\mathrm{Real}\left[\frac{2\bar{T}}{\gamma M^2_\infty \bar{\rho}}\tilde{\rho}^\dagger \tilde{v}\frac{\partial \bar{\rho}}{\partial \eta}\right] \tag{3.10}$$

are significantly more prominent than others for all the cases. For the low-frequency candidate initiated by the inlet perturbation, these three terms all immediately undergo a sharp rise near the inlet, followed by a rapid decay towards a moderate level further downstream. The Reynolds tress term Π^U_{uv} encompassing the lift-up effect remains the largest as expected, while the energy transfer associated with the temperature wall-normal gradient is also non-negligible. Interestingly, another Reynolds stress term, $\Pi^U_{wv} \sim \rho\tilde{w}^\dagger\tilde{v}\partial\bar{w}/\partial\eta + \text{c.c.}$, which is associated with the Orr mechanism in the azimuthal

https://doi.org/10.1017/jfm.2025.199 Published online by Cambridge University Press

direction, manifests itself in the vicinity of the inlet and quickly vanishes downstream. This observation indicates that the azimuthal Orr mechanism, clearly observable in the change of the inclined direction of the streamwise vortices, only moderately promotes the energy growth initially in a direct manner. Nevertheless, the indirect, yet positive influence exerted by the azimuthal Orr mechanism on the lift-up effect through enhancing the crossflow velocities should not be underestimated. Exactly quantifying such indirect effect of the Orr mechanism requires further investigation, which is, however, beyond the scope of the present work.

Clearly, the external forcing tends to primarily transfer energy into the vortex components (especially the azimuthal velocity component) by

$$\Phi_w = \frac{1}{E}\mathrm{Real}\left[\iint \tilde{w}^\dagger \tilde{f}_w \mathrm{d}\eta\, \mathrm{d}\phi\right], \quad \Phi_v = \frac{1}{E}\mathrm{Real}\left[\iint \tilde{v}^\dagger \tilde{f}_v \mathrm{d}\eta\, \mathrm{d}\phi\right], \tag{3.11}$$

which in turn indirectly enhance other primitive components through the lift-up/Orr mechanisms. The contribution of the direct energy transfer from the external forcing rapidly vanishes downstream of the inlet such that the energy transfer distribution closely resembles that of the inlet–outlet optimal growth problem.

Contrarily, for the high-frequency candidate, the Reynolds stress term initially dominates while the temperature energy transfer term Π_v^T rapidly takes over, peaking midway between the inlet and the outlet. The density production term, attaining appreciably large values, evolves similarly to the temperature counterpart. Close inspection of the flow structure displayed in figure 10(d) reveals the coincidence between the peak location of the temperature/density production and the position when the structures turn upright, indicating that these production terms are associated with the (streamwise) Orr mechanism. Intriguingly, although the azimuthally tilted structures as shown in figure 10(b, c) are an indicator of the azimuthal Orr mechanism, the corresponding production term Π_w^T (Π_w^ρ) remains negligibly small. Therefore, whether the azimuthal Orr mechanism is (dynamically) active in the energy growth of the high-frequency optimal disturbance is still unclear.

4. Influence of the AoA

In this section, we assess the influence of the AoA on the non-modal growth. The N-factors of optimal disturbances to inlet perturbation for different frequencies in the case of 4° AoA and the case of 6° AoA are displayed in figures 14(a) and 14(b), respectively. For whatever AoA, the optimal inlet position remains at around $X^* = 44$ mm where the optimal disturbance achieves the largest energy growth, and the outlet position beyond the strong wavemaker region does not modify the evolution path except for raising the final energy gain reached by the disturbance (not shown here). Therefore, we only present the optimal growth results for the spatial interval of $X^* \in (44, 250)$ mm here. Notably, the optimal disturbances in all three cases share qualitatively the same evolution path consisting of the algebraic growth stage (stage I) insensitive to the disturbance frequency and the following quasi-exponential growth stage (stage II) with growth rates relying on the disturbance frequency. Moreover, the most amplified frequency is always around 20 kHz. As shown in figure 14(c), increasing the AoA does not change the growth rate in the algebraic growth stage, but considerably enhances the disturbance amplification in stage II in accord with the strengthening of the crossflow velocity and thus the crossflow instability. Moreover, a larger AoA yields a more pronounced separation of the inlet and outlet disturbance profiles in the azimuthal direction (figure 14d–f), with the inlet disturbance being closer to the windward ray and the outlet disturbance being closer to the leeward

https://doi.org/10.1017/jfm.2025.199 Published online by Cambridge University Press

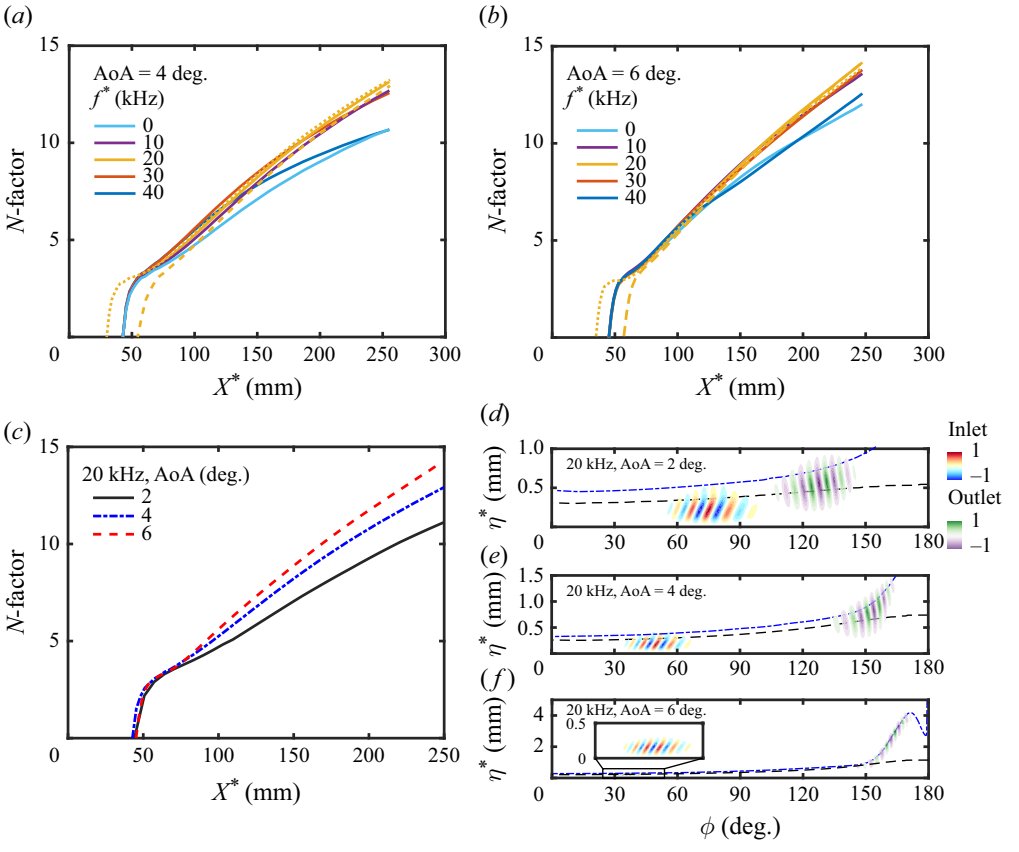


Figure 14. Comparison of N-factor of the optimal disturbance at frequency ranging from $f^* = 0$ to $f^* = 40$ kHz for cases of 4° AoA (*a*) and of 6° AoA (*b*), and at a frequency of 20 kHz for all three cases (*c*). The dashed lines in (*a*,*b*) show the results obtained with suboptimal inlet positions. (*d–f*) The corresponding real part of the temperature disturbance component at the inlet (red–blue contour with dashed lines denoting the boundary-layer edge) and outlet (green–purple contour with dashed-dotted lines denoting the boundary-layer edge).

ray. This obviously stems from the stronger crossflow velocity pertaining to a larger AoA and implies an increasingly important role played by the azimuthal crossflow instability mechanism in the optimal growth.

The AoA effects on the evolution path and azimuthal wavenumber of the 20 kHz optimal disturbance are illustrated in figure 15. Here, the disturbance path is sketched by the distribution of the wall-normal integrated Chu energy normalised by the local maximum value along the azimuthal direction. The azimuthal wavenumber is obtained by the Fourier transform of the wall density perturbations. It is seen that the disturbance path initiated from the windward to leeward side becomes more tilted at higher AoA as expected. More interestingly, the dominant azimuthal wavenumbers remain at $n \approx 40-50$ except for the highest AoA case where they initially take higher values. Note that approaching the outlet, a lower azimuthal wavenumber peak arises in figure 15(*f*) because the optimal disturbance penetrates into the vortex region as is shown later. The optimal stationary disturbance results quantitatively resemble the travelling disturbance results. Notably, previous numerical (Li *et al.* 2010) as well as experimental (Swanson & Schneider 2010; Schuele *et al.* 2013; Corke *et al.* 2018) studies have documented a dominant azimuthal

https://doi.org/10.1017/jfm.2025.199 Published online by Cambridge University Press

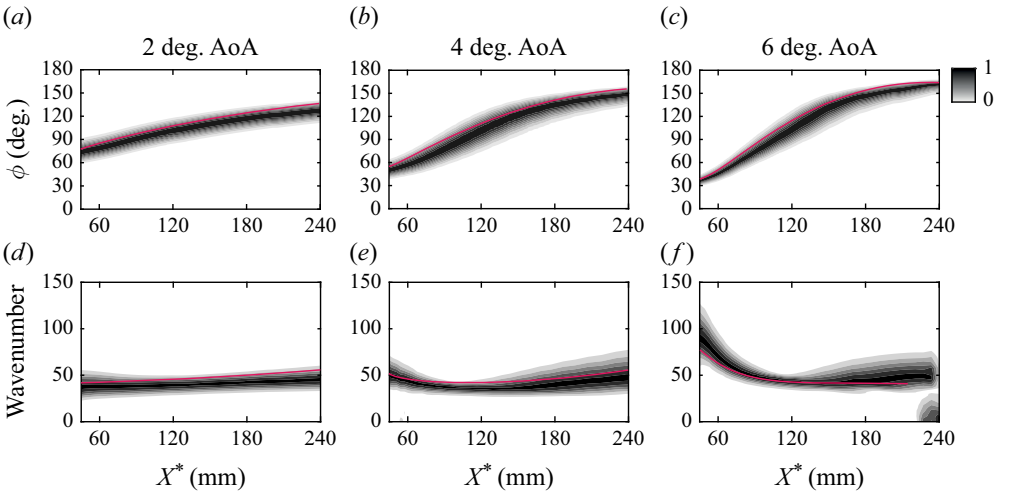


Figure 15. Streamwise evolution of the normalised disturbance energy distribution (*a–c*) and the normalised azimuthal wavenumber distribution obtained by the wall density perturbations (*d–f*) of the 20 kHz optimal disturbances for different cases: (*a*, *d*) 2° AoA, (*b*, *e*) 4° AoA and (*c*, *f*) 6° AoA. The peak locations of the corresponding results for the stationary optimal disturbances are also displayed by red lines.

wavenumber range of crossflow disturbances very close to that of the present study despite rather different cone models and flow parameters.

The spatial structures of the most amplified optimal disturbances for three cases are compared in figure 16, featuring the tilted streaks on the cone surface with larger inclined angles for increasing AoA. It is instructive to compare the optimal amplitude envelopes with the modal counterpart calculated, respectively, by PSE3D and LST. All methods predict stronger disturbance energy growth with increasing AoA, as expected. Again, the optimal disturbance is remarkably more amplified than the 2-D local modal counterpart, but such superiority quickly diminishes as the AoA increases. This is because increasing AoA greatly promotes the modal instability yet barely affects the algebraic growth, and as such, the modal instability becomes increasingly important. The N-factors based on LST (1-D analysis) are significantly larger than those of 2-D local modes and even surpass the optimal ones at high AoA. Aside from the N-factor, the amplitude envelopes from the three also differ in terms of the peak position in the azimuthal direction: the 2-D local modal amplitude envelope lies closest to the leeward ray, followed by the local one and the global optimal one.

Intriguingly, the optimal disturbance at 6° AoA has penetrated partly into the leeward vortex region, which likely interferes with or even precipitates the transition process therein as documented by Wang *et al.* (2023) in a numerical study on a similar flow configuration. Quintanilha *et al.* (2022) reported that the temporal optimal crossflow disturbances on a hypersonic elliptic cone ultimately reside in the vortex region, manifesting as intrinsic vortex modes. In this study, however, we find that the optimal disturbance preserves the crossflow-instability feature towards the outlet rather than develops into an intrinsic vortex instability. To show this, in figure 17 we display the eigenspectrum of 20 kHz modes obtained by 2-D LST for one representative streamwise station ($X^* = 208$ mm), along with the typical spatial distributions of the modes. One can distinguish two types of instabilities, i.e. the crossflow instability consisting of many modes in the phase velocity range of $(0.1–0.4)U_\infty$ and the vortex instability containing few modes with higher phase velocities. Comparison of figure 17(*b–d*) and figure 14(*f*) clearly

https://doi.org/10.1017/jfm.2025.199 Published online by Cambridge University Press

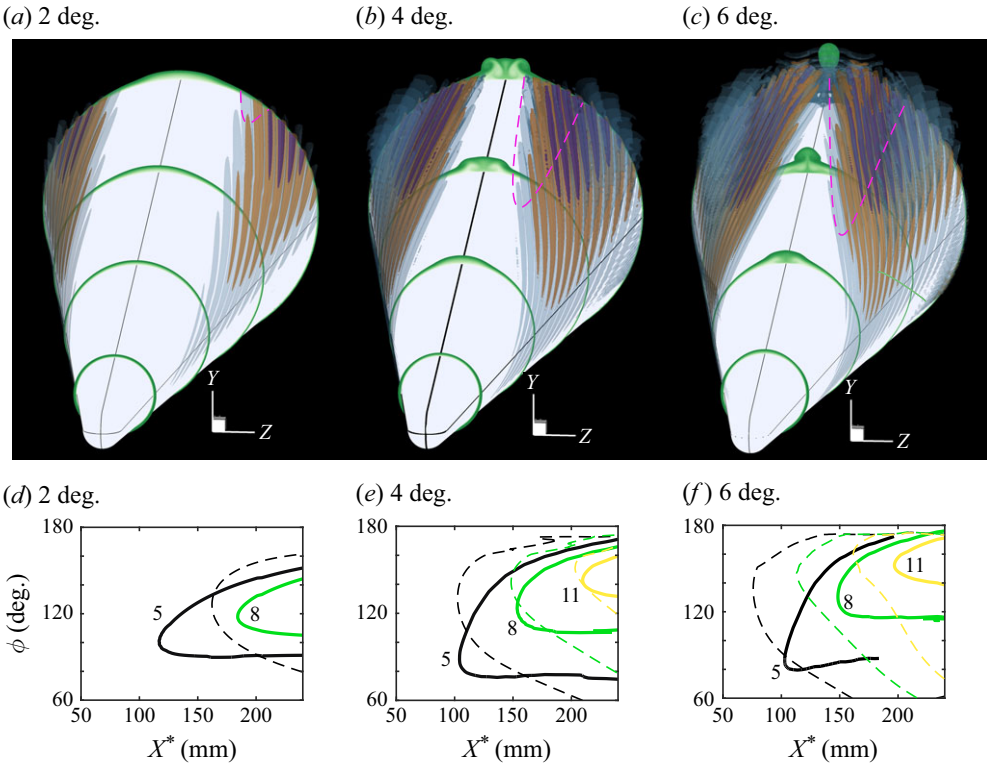


Figure 16. (a–c) Spatial structures of the optimal disturbance at 20 kHz for three AoA, visualised by three isosurfaces, $N_T = 5$ (blue), $N_T = 8$ (orange) and $N_T = 11$ (purple), of the real part of temperature disturbances normalised by the maximum value at the initial profile for each case. The PSE3D N-factor envelope ($N = 2.3$ pink dashed line) initiated by the most amplified 2-D local crossflow mode is also displayed. (d–f) The corresponding N_{Chu}-factor isolines (black: $N_{Chu} = 5$; green: $N_{Chu} = 8$; yellow: $N_{Chu} = 11$) in the X^*–ϕ plane, along with the LST-eN results (dashed lines).

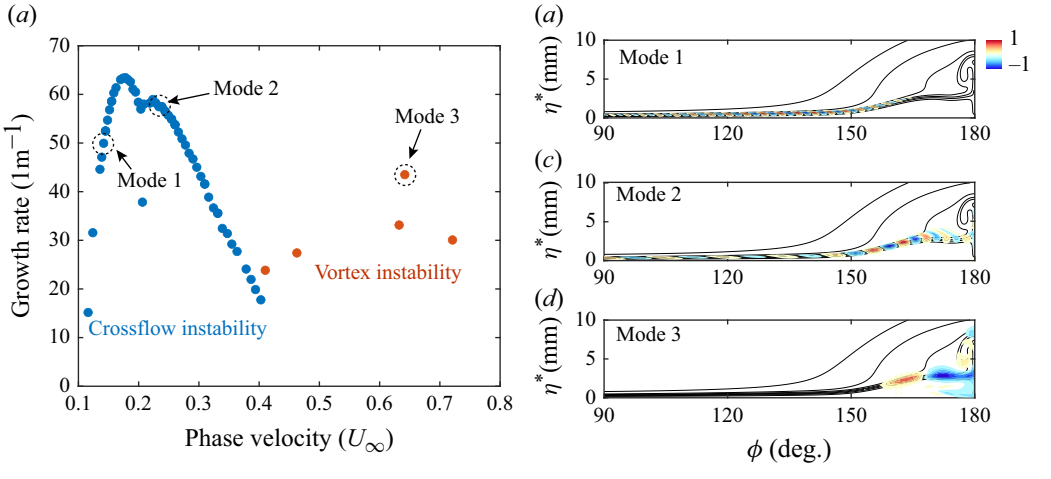


Figure 17. (a) Eigenspectrum for a frequency of 20 kHz for the case of 6° AoA at $X^* = 208$ mm. The blue circles designate the crossflow modes and the red circles stand for the intrinsic vortex modes. (b–d) The real parts of the normalised temperature shape functions of three representative modes, overlayed with the temperature isolines of the base flow.

https://doi.org/10.1017/jfm.2025.199 Published online by Cambridge University Press

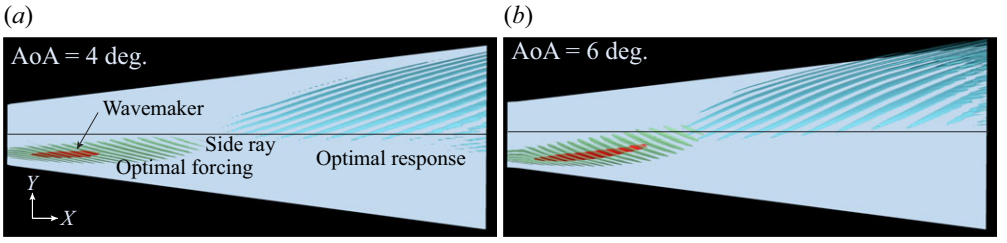


Figure 18. Spatial structure of the optimal forcing (green, energy equation forcing $\mathrm{Re}(\hat{f}_T) = 10^{-5}$), the optimal response (blue, temperature component $\mathrm{Re}(\hat{T}) = 50\,000$) and the resolvent wavemaker (red, $0.5|\Lambda|_{max}$) for two AoA: (*a*) 4°; (*b*) 6°.

confirms the crossflow instability nature of the optimal disturbance. This is reasonable since the crossflow instability is more unstable than the vortex instability and the optimal disturbance should thus take advantage of the former to achieve the optimal spatial growth.

In summary, increasing the AoA simply enhances the modal instability, resulting in a more pronounced azimuthal shift of the disturbance, yet exerts relatively small influence on the initial algebraic growth. This observation also holds true for the optimal response to external forcing. For brevity, we only present the spatial structures of the optimal forcing/response and the wavemaker for the two higher AoA cases in figure 18, showing essentially the same pattern as in the case of 2° AoA in figure 12.

5. Conclusions and discussion

In this work, the optimal responses to the inlet disturbances and the external forcing in the entire domain are investigated within a uniform input–output framework for hypersonic boundary layers on a blunt cone at non-zero AoA. Well-established parabolised governing equations (PSE3D and APSE3D) are employed to efficiently obtain the spatial evolution of direct as well as adjoint states, which allows for a systematic parameter study. Comparisons with relevant literature data and other sophisticated numerical tools including HLNS and direct numerical simulation (DNS) demonstrate the reliability of the present solver in calculating the non-modal disturbances.

The optimal growth analysis seeking the optimal response to inlet perturbation is first conducted for the case with 2° AoA, which lays the foundation for finding the optimal response to external forcing and subsequent study of the effects of AoA. The optimal disturbances, peaking at 20 kHz, initially take the form of azimuthally compact tilted streamwise vortices on the windward side. While convected downstream, they quickly rise to an upright position and give rise to bent streaks, accompanied by a substantial energy growth. The initial phase of energy growth is algebraic, attributed to a combination of the lift-up effect and the Orr mechanism, and is later smoothly replaced by an exponential-like growth primarily driven by the crossflow-instability mechanism. Such a two-stage growth process bears a strong resemblance to what has been observed by Tempelmann *et al.* (2010,2012) in an infinite SWBL. However, we note two important differences caused by the azimuthal inhomogeneity in the present configuration. Firstly, instead of following a single crossflow mode as in the SWBL case, the optimal disturbance in the second stage behaves more like a non-modal one comprised of several leading 2-D local crossflow modes, and thus amplifies much faster than does the most unstable crossflow mode. Secondly, the optimal disturbances are localised in the azimuthal direction rather than uniformly distributed in the SWBL case, and shift azimuthally from the windward side towards the leeward ray while travelling downstream such that they can exploit the

https://doi.org/10.1017/jfm.2025.199 Published online by Cambridge University Press

crossflow-instability mechanism not only along the streamwise direction but also along the azimuthal direction. This spatial movement of the disturbance structure prevails in the 2-D streamwise global non-modal analyses and is known to stem from the combination of multiple global modes (Chomaz 2005). Increasing the AoA barely affects the algebraic growth stage, yet substantially promotes the exponential growth through strengthening the crossflow instability, leading to a more prominent azimuthal shift of the disturbance structure.

The structural sensitivity (wavemaker) of the optimal gain is shown to be quantified by the pointwise product between the direct and adjoint (or forcing) states. Our results indicate that the wavemakers of low-frequency optimal disturbances always reside on the windward side immediately downstream of the inlet position where efficient transition control might be implemented.

The optimal external forcing concentrates in the vicinity of the inlet with amplitude rapidly decaying downstream. The azimuthal and wall-normal forces are dominant components that are expected to enhance the Orr and lift-up mechanisms. The resulting optimal response, also peaking at 20 kHz, is essentially the same as the optimal growth disturbance mentioned above except that the initial algebraic growth becomes more pronounced due to external forces.

We have also discovered relatively weaker, yet broadband high-frequency optimal growth disturbances that preferentially reside between the boundary layer and the entropy layer on the windward side. They are initially tilted against both the azimuthal and streamwise flow directions, but their orientation with respect to the surface gradually rotates to the opposite direction, suggesting an Orr-like mechanism that mainly amplifies the temperature component of the disturbance.

Energy transfer analysis identifies the dominant role played by the production terms associated with the wall-normal shear in the optimal growth process.

Finally, we have drawn a comparison between the optimal growth initiated by the inlet profile and the modal growth obtained separately from 1-D local (LST) and multi-dimensional (global) stability (PSE3D) analyses. The results from various approaches turn out to differ significantly in terms of the N-factor (optimal disturbance reaches the maximum followed by the 1-D and multi-dimensional modal disturbances) as well as the amplitude envelope shape (transition front), highlighting the caution required in choosing the stability analysis tool in employing the eN transition prediction method. While local analysis is deemed unable to retrieve the disturbance structures and to tackle the nonlinear interactions of disturbances in a truly 3-D boundary layer, tracing a multi-dimensional mode is of little importance too given the high sensitivity and multiplicity of crossflow eigenvalues (Chen *et al.* 2022), especially when characterising the transition mechanism under noisy free-stream conditions (e.g. in a conventional wind tunnel). Alternatively, the optimal solution serves as a robust and physically meaningful representation of the crossflow instability, offering a starting point for investigating the nonlinear development and the ensuing breakdown process of crossflow-instability disturbances from a global perspective, and, moreover, provides an upper bound on the linear growth experienced by disturbances.

However, the link between the real free-stream disturbances and the optimal profiles is not addressed herein. The recent DNS performed by Liu *et al.* (2022*b*) and Schuabb *et al.* (2024) for an axisymmetric blunt cone showed that the 'tunnel-like' acoustic disturbance field, which faithfully models the real wind-tunnel noise, could trigger prominent entropy-layer disturbances resembling the predictions of optimal growth (Paredes *et al.* 2020). Their results give confidence that the optimal disturbances are physically realisable. Another important issue that warrants further investigation is determining whether the

https://doi.org/10.1017/jfm.2025.199 Published online by Cambridge University Press

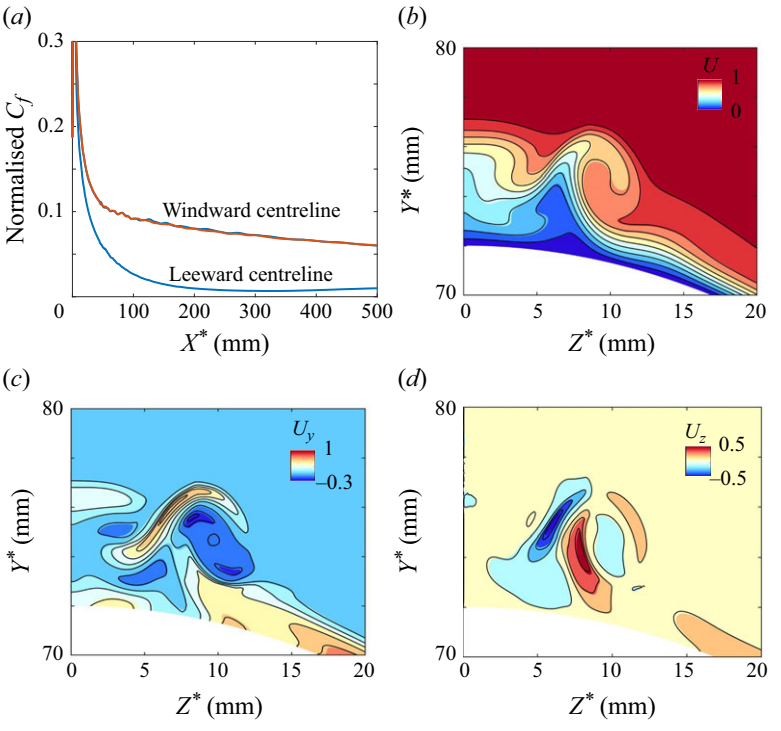


Figure 19. Convergence test for the base flow of the 2° AoA case with the baseline grid ($N_\xi \times N_\eta \times N_\phi = 501 \times 301 \times 301$) and the refined grid ($N_\xi \times N_\eta \times N_\phi = 501 \times 351 \times 351$). (*a*) The normalised skin friction coefficient C_f along the windward and leeward centrelines (blue: baseline grid; red: fine grid). The isolines (from the baseline grid) and colour contours (from the fine grid) of (*b*) the velocity $\bar{U}$, (*c*) the vertical shear $\partial U/\partial Y$ and (*d*) the azimuthal shear $\partial U/\partial Z$ for the vortex region at $X^* = 550$ mm.

present 3-D boundary layer is a low-rank (i.e. with a large gain separation between optimal and suboptimal disturbances) system similar to the 2-D counterpart (Luchini 2000). If so, even though the real disturbances have a small fraction of their energy in the optimal perturbation, one could still expect to observe a response like the optimal one, which would markedly benefit the transition prediction.

Acknowledgements. The authors appreciate the useful comments from the anonymous referees.

Funding. This work was supported by the National Natural Science Foundation of China through grants 12372225 and 12272395.

Declaration of interests. The authors report no conflict of interest.

Appendix A. Convergence test of the base flow calculation

The base-flow computation strategy used in the present study has been well verified in a similar flow configuration (Li *et al.* 2020). In this appendix, we further present the convergence test results for the case of the 2° AoA. Compared with the baseline grid ($N_\xi \times N_\eta \times N_\phi = 501 \times 301 \times 301$), the refined grid ($N_\xi \times N_\eta \times N_\phi = 501 \times 351 \times 351$) has slightly more grid points in the wall-normal and azimuthal directions along which the base flow varies more significantly than the streamwise direction. As evident in figure 19, the results from the two grids are nearly indistinguishable in terms of the skin friction along the windward/leeward centreline and the leeward vortex profile along with the shear

https://doi.org/10.1017/jfm.2025.199 Published online by Cambridge University Press

distribution which are deemed most sensitive to the grid resolution. Note that although the present stability analyses are all performed in the region before $X^* < 300$ mm, we have made a comparison at a station ($X^* = 550$ mm) much downstream so that the vortex structure is more developed and is thus more representative of the other two base flow cases with larger AoA.

Appendix B. Derivation of the wavemaker

Following the methodology of Schmid & Brandt (2014), we consider base-flow perturbation of operators in (2.21) and (2.27), which reads

$$\delta\mathcal{P}^\dagger\hat{\boldsymbol{p}} + \mathcal{P}^\dagger\delta\hat{\boldsymbol{p}} = \delta\boldsymbol{M}\mathcal{D}\hat{\boldsymbol{q}} + \boldsymbol{M}\mathcal{D}\delta\hat{\boldsymbol{q}}, \tag{B1}$$

$$\delta\mathcal{P}\hat{\boldsymbol{q}} + \mathcal{P}\delta\hat{\boldsymbol{q}} = -\frac{\delta\lambda}{\lambda^2}\boldsymbol{Q}^{-1}\mathcal{C}\hat{\boldsymbol{p}} + \frac{1}{\lambda}\boldsymbol{Q}^{-1}\mathcal{C}\delta\hat{\boldsymbol{p}} + \frac{1}{\lambda}\delta(\boldsymbol{Q}^{-1})\mathcal{C}\hat{\boldsymbol{p}}. \tag{B2}$$

Here, $\delta(*)$ represents small perturbation, and should not be confused with the Dirac delta function. Left-multiplying (B1) by $\hat{\boldsymbol{q}}^\dagger$ and (B2) by $\hat{\boldsymbol{p}}^\dagger$, respectively, yields

$$(\hat{\boldsymbol{q}}, \delta\mathcal{P}^\dagger\hat{\boldsymbol{p}}) + (\hat{\boldsymbol{q}}, \mathcal{P}^\dagger\delta\hat{\boldsymbol{p}}) = (\hat{\boldsymbol{q}}, \delta\boldsymbol{M}\mathcal{D}\hat{\boldsymbol{q}}) + (\hat{\boldsymbol{q}}, \boldsymbol{M}\mathcal{D}\delta\hat{\boldsymbol{q}}), \tag{B3}$$

$$(\hat{\boldsymbol{p}}, \delta\mathcal{P}\hat{\boldsymbol{q}}) + (\hat{\boldsymbol{p}}, \mathcal{P}\delta\hat{\boldsymbol{q}}) = -\left(\hat{\boldsymbol{p}}, \frac{\delta\lambda}{\lambda^2}\boldsymbol{Q}^{-1}\mathcal{C}\hat{\boldsymbol{p}}\right) + \left(\hat{\boldsymbol{p}}, \frac{1}{\lambda}\boldsymbol{Q}^{-1}\mathcal{C}\delta\hat{\boldsymbol{p}}\right) + \left(\hat{\boldsymbol{p}}, \frac{1}{\lambda}\delta\boldsymbol{Q}^{-1}\mathcal{C}\hat{\boldsymbol{p}}\right). \tag{B4}$$

Summing (B3) and (B4) to eliminate the terms associated with the perturbed shape functions, i.e. $\delta\hat{\boldsymbol{q}}$ and $\delta\hat{\boldsymbol{p}}$, by employing the direct and adjoint equations (2.21) and (2.27), leads to

$$(\hat{\boldsymbol{q}}, \delta\mathcal{P}^\dagger\hat{\boldsymbol{p}}) + (\hat{\boldsymbol{p}}, \delta\mathcal{P}\hat{\boldsymbol{q}}) = (\hat{\boldsymbol{q}}, \delta\boldsymbol{M}\mathcal{D}\hat{\boldsymbol{q}}) + \left(\hat{\boldsymbol{p}}, \frac{1}{\lambda}\delta\boldsymbol{Q}^{-1}\mathcal{C}\hat{\boldsymbol{p}}\right) - \left(\hat{\boldsymbol{p}}, \frac{\delta\lambda}{\lambda^2}\boldsymbol{Q}^{-1}\mathcal{C}\hat{\boldsymbol{p}}\right). \tag{B5}$$

By substituting (2.22) into (B5), and remembering the projector feature and the forcing amplitude constraint, (B5) can be further simplified to

$$2\mathrm{Re}(\hat{\boldsymbol{p}}, \delta\mathcal{P}\hat{\boldsymbol{q}}) = -\delta\lambda + (\hat{\boldsymbol{q}}, \delta\boldsymbol{M}\mathcal{D}\hat{\boldsymbol{q}}) + (\hat{\boldsymbol{p}}, \frac{1}{\lambda}\delta\boldsymbol{Q}^{-1}\mathcal{C}\hat{\boldsymbol{p}}), \tag{B6}$$

or equivalently

$$2\mathrm{Re}(\hat{\boldsymbol{f}}, \delta\mathcal{P}\hat{\boldsymbol{q}}) = \frac{-\delta\lambda}{\lambda} + \frac{1}{\lambda}(\hat{\boldsymbol{q}}, \delta\boldsymbol{M}\mathcal{D}\hat{\boldsymbol{q}}) + \left(\hat{\boldsymbol{p}}, \frac{1}{\lambda^2}\delta\boldsymbol{Q}^{-1}\mathcal{C}\hat{\boldsymbol{p}}\right). \tag{B7}$$

Therefore, we obtain the changes of the optimal gain to perturbation of base flow as

$$\delta\lambda = -2\mathrm{Re}(\hat{\boldsymbol{p}}, \delta\mathcal{P}\hat{\boldsymbol{q}}) + (\hat{\boldsymbol{q}}, \delta\boldsymbol{M}\mathcal{D}\hat{\boldsymbol{q}}) + \left(\hat{\boldsymbol{p}}, \frac{1}{\lambda}\delta\boldsymbol{Q}^{-1}\mathcal{C}\hat{\boldsymbol{p}}\right) \tag{B8}$$

$$= -2\mathrm{Re}(\hat{\boldsymbol{f}}, \delta\mathcal{P}\hat{\boldsymbol{q}})\lambda + (\hat{\boldsymbol{q}}, \delta\boldsymbol{M}\mathcal{D}\hat{\boldsymbol{q}}) + \left(\hat{\boldsymbol{p}}, \frac{1}{\lambda}\delta\boldsymbol{Q}^{-1}\mathcal{C}\hat{\boldsymbol{p}}\right). \tag{B9}$$

The terms $(\hat{\boldsymbol{q}}, \delta\boldsymbol{M}\mathcal{D}\hat{\boldsymbol{q}})$ and $(\hat{\boldsymbol{p}}, \frac{1}{\lambda}\delta\boldsymbol{Q}^{-1}\mathcal{C}\hat{\boldsymbol{p}})$ simply reflect the changes related to the energy weight, while the first term on the right-hand side indicates that the important structural-sensitivity region corresponds to the overlap regions of the adjoint variable (forcing) and the response. By neglecting the trivial terms pertaining to the energy weight, we can derive a bound for the gain drift under a unit-norm perturbation $\|\delta\mathcal{P}\| = 1$ as

$$|\delta\lambda| \leqslant 2\int \|\hat{\boldsymbol{q}}\|\|\hat{\boldsymbol{p}}\|\mathrm{d}\Omega = 2\lambda\int \|\hat{\boldsymbol{q}}\|\|\hat{\boldsymbol{f}}\|\mathrm{d}\Omega, \tag{B10}$$

https://doi.org/10.1017/jfm.2025.199 Published online by Cambridge University Press

Case	Model	Ma	Re_0 (X_0^*)	Re_1 (X_1^*)	T_w^* (K)	T_0^* (K)	$F \times 10^6$ (f^*)	β
A1	Flat plate	0.001	0	10 000	None	333	0	Varying
A2	Flat plate	3	500	1000	Adiabatic	333	0	Varying
A3	Flat plate	6	500	1000	$T_w/T_{ad} = 0.8$	333	0	Varying
B1	Flat plate	6	500	707	Adiabatic	430	0	0.1
B2	Flat plate	6	500	707	Adiabatic	430	200	0.1
B3	Flat plate	6	500	707	Adiabatic	430	300	0.1
C1	Inclined cone	6	44 mm	275 mm	300	501	3.3 (20 kHz)	—
C2	Inclined cone	6	44 mm	275 mm	300	501	8.3 (50 kHz)	—
C3	Inclined cone	6	44 mm	212 mm	300	501	33 (200 kHz)	—

Table 1. Nine cases of three groups are considered for the verification of the PSE methodology in optimal disturbance calculations.

where $\|\cdot\|$ should be understood as the pointwise norm of the mode. For example,

$$\|\hat{\boldsymbol{q}}(\xi, \eta, \phi)\|^2 \equiv |\hat{u}(\xi, \eta, \phi)|^2 + |\hat{v}(\xi, \eta, \phi)|^2 + |\hat{w}(\xi, \eta, \phi)|^2 + |\hat{\rho}(\xi, \eta, \phi)|^2 + |\hat{T}(\xi, \eta, \phi)|^2. \tag{B11}$$

The wavemaker Λ is then defined as

$$\Lambda \equiv \|\hat{\boldsymbol{q}}\| \|\hat{\boldsymbol{p}}\| = \lambda \|\hat{\boldsymbol{q}}\| \|\hat{\boldsymbol{f}}\|. \tag{B12}$$

Appendix C. Verification of optimal growth calculation

The PSE method specifies a single streamwise wavenumber in order to absorb the main streamwise oscillations of the disturbances into the exponential term, thereby keeping the shape function slowly varying. This casts doubt on whether the PSE method is able to accurately trace the evolution of non-modal disturbances inherently consisting of many modes with varying streamwise wavenumbers (Towne *et al.* 2019), although the PSE method and its variant have been widely employed in non-modal studies (e.g. Levin & Henningson 2003; Guegan *et al.* 2008; Tempelmann *et al.* 2010, 2012; Paredes *et al.* 2020). In order to assess the effects exerted by the PSE method on the optimal growth, we have examined nine cases of three groups as shown in table 1. The cases from the first group come from Paredes *et al.* (2016*a*) who considered the optimal growth for stationary disturbances over a flat-plate boundary layer at several Mach numbers. The second group is to test the ability of the PSE methodology in accurately capturing the non-stationary optimal disturbances by comparing with results of the HLNS equations which retain all the elliptic effects. Particularly, the B3 case lies in the second Mack mode regime, and is the most challenging one of the first two groups. Finally, we used DNS to calculate the spatial evolution of the optimal disturbance for three frequencies over the inclined cone at 2° AoA studied in the present work to directly verify the ability of PSE3D in tracing a non-modal disturbance in a 3-D boundary layer.

The optimal energy gains for the first two groups are displayed in figure 20. It can be seen that the agreement between the present PSE results and the literature results in figure 20(*a*), as well as the HLNS results in figure 20(*b*), is satisfactory. The fluctuation contours in case B3 are further compared in figure 21. Again, good agreement between HLNS results and PSE results is observed for the temperature disturbance except for marginal differences in the free-stream region. This is reasonable because the free-stream disturbances (mainly consisting of acoustic waves) and the fluctuations within the boundary layer have substantially different streamwise wavenumbers (or phase velocities),

https://doi.org/10.1017/jfm.2025.199 Published online by Cambridge University Press

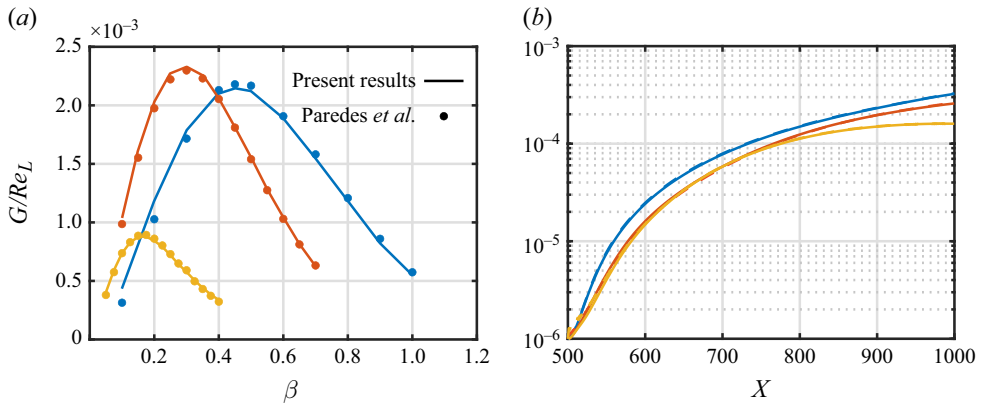


Figure 20. (*a*) Comparison with optimal gain predictions by Paredes *et al.* (2016*a*) for flat-plate boundary layers at Mach 0.001 (blue, case A1), 3 (red, case A2) and 6 (yellow, case A3). (*b*) Comparison of the disturbance energy evolution optimised in the range of $X \in (500, 1000)$ by the PSE methodology (solid lines) and the HLNS methodology (dashed lines) for three frequencies: $F = 0$ (blue, case B1), $F = 2 \times 10^{-4}$ (red, case B2) and $F = 3 \times 10^{-4}$ (yellow, case B3) at the Mach 6 adiabatic flat-plate boundary layer.

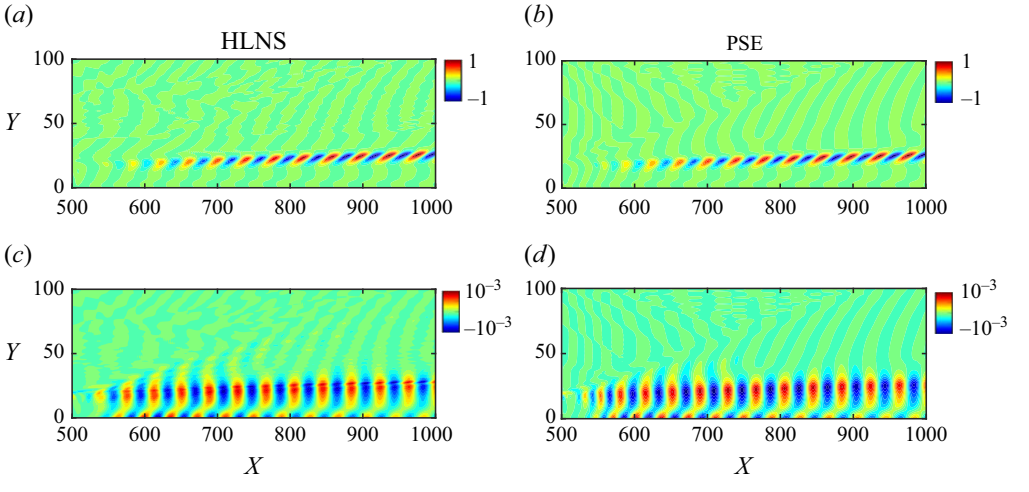


Figure 21. Contours of the optimal disturbance normalised by the temperature component for case B3: (*a*, *c*) HLNS results; (*b*, *d*) PSE results. (*a*, *b*) Temperature fluctuation; (*c*, *d*) pressure fluctuation.

and might thus not be captured by PSE simultaneously. Compared with the temperature fluctuations, the pressure fluctuations exhibit slightly larger differences, as was also documented by Towne *et al.* (2019). This is because the pressure disturbance amplitude is about three orders of magnitude smaller than the temperature disturbance amplitude and small discrepancies in temperature would appear more pronounced in pressure. Since the pressure and free-stream disturbances play a secondary role in the non-modal growth process as shown above (see also Hanifi *et al.* (1996) who noted that the acoustic continuous branches do not contribute to the transient growth of the energy), such discrepancies do not affect the main results of the non-modal analyses.

Finally, we present in figure 22 the direct comparison between results from DNS and PSE3D for the last group of test cases. The DNS computation domain is the same as that of PSE3D. The DNS grid is $N_\xi \times N_\eta \times N_\phi = 1001 \times 201 \times 401$ for the lowest

https://doi.org/10.1017/jfm.2025.199 Published online by Cambridge University Press

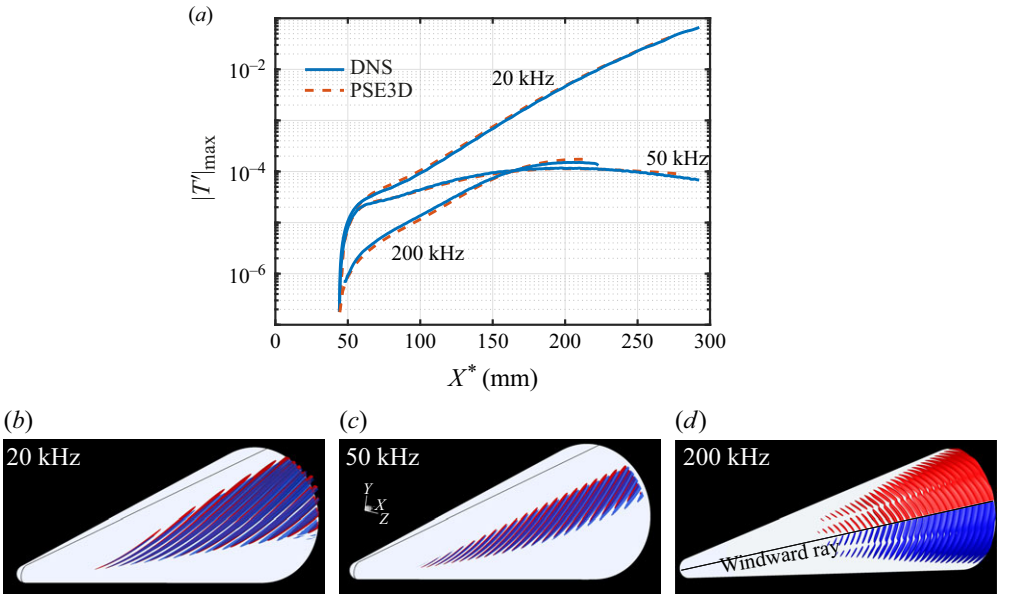


Figure 22. Verification of PSE3D results by DNS for the optimal disturbances at 20, 50 and 200 kHz over the inclined cone at 2° AoA. The initial amplitude of DNS is prescribed to a small value to ensure linearity. (*a*) Temperature disturbance amplitude evolution. (*b–d*) Temperature disturbance isosurfaces normalised by the initial amplitude for the three cases (red: DNS; blue: PSE3D, $\mathrm{Re}(\hat{T}) = 100$ for (*b*, *c*) and $\mathrm{Re}(\hat{T}) = 13$ for (*d*)).

frequency (most amplified one), $N_\xi \times N_\eta \times N_\phi = 1201 \times 201 \times 501$ for the moderate one and $N_\xi \times N_\eta \times N_\phi = 1401 \times 301 \times 401$ for the highest one, with slightly more grid points being distributed in the leeward vortex region. Evidently, results from these two approaches match well in terms of the amplitude evolution as well as the spatial structures, thus verifying the PSE3D results.

Appendix D. Entries of linear operators in PSE3D

The non-zero elements of coefficient matrices $\boldsymbol{A}$, $\boldsymbol{B}$ in (2.39) are as follows. Note that the overbar of the base-flow quantities has been omitted for simplicity:

$$\boldsymbol{A}(1,1) = U\mathcal{D}_x + V\mathcal{D}_y + W\mathcal{D}_z + U_x + V_y + W_z - i\omega, \tag{D1}$$

$$\boldsymbol{A}(1,2) = \rho_x + \rho\mathcal{D}_x, \tag{D2}$$

$$\boldsymbol{A}(1,3) = \rho_y + \rho\mathcal{D}_y, \tag{D3}$$

$$\boldsymbol{A}(1,4) = \rho_z + \rho\mathcal{D}_z, \tag{D4}$$

$$\boldsymbol{A}(2,1) = (T\mathcal{D}_x + T_x)/(\gamma M_\infty^2) + UU_x + VU_y + WU_z, \tag{D5}$$

$$\begin{aligned}\boldsymbol{A}(2,2) = &-\mu/R(\mathcal{D}_{yy} + \mathcal{D}_{zz} + l_2\mathcal{D}_{xx}) + \rho(U_x - i\omega) + (\rho U - l_2\mu_x/R)\mathcal{D}_x \\ &+ (\rho V - \mu_y/R)\mathcal{D}_y + (\rho W - \mu_z/R)\mathcal{D}_z,\end{aligned} \tag{D6}$$

$$\boldsymbol{A}(2,3) = -l_1\mu/R\mathcal{D}_x\mathcal{D}_y - l_0\mu_x/R\mathcal{D}_y - \mu_y/R\mathcal{D}_x + \rho U_y, \tag{D7}$$

https://doi.org/10.1017/jfm.2025.199 Published online by Cambridge University Press

$$\boldsymbol{A}(2,4) = -l_1\mu/R\mathcal{D}_x\mathcal{D}_z - l_0\mu_x/R\mathcal{D}_z - \mu_z/R\mathcal{D}_x + \rho U_z, \tag{D8}$$

$$\begin{aligned}\boldsymbol{A}(2,5) = {}& (\rho\mathcal{D}_x + \rho_x)/(\gamma M_\infty^2) - \mu_T/R(l_2U_x + l_0V_y + l_0W_z)\mathcal{D}_x - \mu_T/R(U_z + W_x)\mathcal{D}_z \\ & - \mu_T/R(U_y + V_x)\mathcal{D}_y - \mu_T/R(l_1V_{xy} + l_1W_{xz} + U_{zz} + U_{yy} + l_2U_{xx}) \\ & - \mu_{TT}/R\{(U_z + W_x)T_z + (V_x + U_y)T_y + (l_0V_y + l_0W_z + l_2U_x)T_x\},\end{aligned} \tag{D9}$$

$$\boldsymbol{A}(3,1) = (T\mathcal{D}_y + T_y)/(\gamma M_\infty^2) + UV_x + VV_y + WV_z, \tag{D10}$$

$$\boldsymbol{A}(3,2) = -l_1\mu/R\mathcal{D}_x\mathcal{D}_y - \mu_x/R\mathcal{D}_y - l_0\mu_y/R\mathcal{D}_x + \rho V_x, \tag{D11}$$

$$\begin{aligned}\boldsymbol{A}(3,3) = {}& -\mu/R(l_2\mathcal{D}_{yy} + \mathcal{D}_{zz} + \mathcal{D}_{xx}) + \rho(U_y - i\omega) + (\rho U - \mu_x/R)\mathcal{D}_x \\ & + (\rho V - l_2\mu_y/R)\mathcal{D}_y + (\rho W - \mu_z/R)\mathcal{D}_z,\end{aligned} \tag{D12}$$

$$\boldsymbol{A}(3,4) = -l_1\mu/R\mathcal{D}_z\mathcal{D}_y - \mu_z/R\mathcal{D}_y - l_0\mu_y/R\mathcal{D}_z + \rho V_z, \tag{D13}$$

$$\begin{aligned}\boldsymbol{A}(3,5) = {}& (\rho\mathcal{D}_y + \rho_y)/(\gamma M_\infty^2) - \mu_T/R(l_0U_x + l_2V_y + l_0W_z)\mathcal{D}_y - \mu_T/R(V_z + W_y)\mathcal{D}_z \\ & - \mu_T/R(U_y + V_x)\mathcal{D}_x - \mu_T/R(l_1U_{xy} + l_1W_{yz} + V_{zz} + l_2V_{yy} + V_{xx}) \\ & - \mu_{TT}/R\{(V_z + W_y)T_z + (V_x + U_y)T_x + (l_2V_y + l_0W_z + l_0U_x)T_y\},\end{aligned} \tag{D14}$$

$$\boldsymbol{A}(4,1) = (T\mathcal{D}_z + T_z)/(\gamma M_\infty^2) + UW_x + VW_y + WW_z, \tag{D15}$$

$$\boldsymbol{A}(4,2) = -l_1\mu/R\mathcal{D}_x\mathcal{D}_z - l_0\mu_z/R\mathcal{D}_x - \mu_x/R\mathcal{D}_z + \rho W_x, \tag{D16}$$

$$\boldsymbol{A}(4,3) = -l_1\mu/R\mathcal{D}_y\mathcal{D}_z - l_0\mu_z/R\mathcal{D}_y - \mu_y/R\mathcal{D}_z + \rho W_y, \tag{D17}$$

$$\begin{aligned}\boldsymbol{A}(4,4) = {}& -\mu/R(\mathcal{D}_{yy} + l_2\mathcal{D}_{zz} + \mathcal{D}_{xx}) + \rho(U_z - i\omega) \\ & + (\rho U - \mu_x/R)\mathcal{D}_x + (\rho V - \mu_y/R)\mathcal{D}_y + (\rho W - l_2\mu_z/R)\mathcal{D}_z,\end{aligned} \tag{D18}$$

$$\begin{aligned}\boldsymbol{A}(4,5) = {}& (\rho\mathcal{D}_z + \rho_z)/(\gamma M_\infty^2) - \mu_T/R(l_0U_x + l_0V_y + l_2W_z)\mathcal{D}_z - \mu_T/R(U_z + W_x)\mathcal{D}_x \\ & - \mu_T/R(W_y + V_z)\mathcal{D}_y - \mu_T/R(l_1U_{xz} + l_1V_{yz} + l_2W_{zz} + W_{yy} + W_{xx}) \\ & - \mu_{TT}/R\{(V_z + W_y)T_y + (U_z + W_x)T_x + (l_0V_y + l_2W_z + l_0U_x)T_z\},\end{aligned} \tag{D19}$$

$$\begin{aligned}\boldsymbol{A}(5,1) = {}& -(\gamma - 1)(UT\mathcal{D}_x + VT\mathcal{D}_y + WT\mathcal{D}_z - i\omega T + UT_x) \\ & + UT_x + VT_y + WT_z,\end{aligned} \tag{D20}$$

$$\begin{aligned}\boldsymbol{A}(5,2) = {}& -2\gamma(\gamma - 1)M_\infty^2\mu/R\{(l_2U_x + l_0V_y + l_0W_z)\mathcal{D}_x + (U_y + V_x)\mathcal{D}_y \\ & + (U_z + W_x)\mathcal{D}_z\} + \gamma\rho T_x + (1 - \gamma)P_x,\end{aligned} \tag{D21}$$

$$\begin{aligned}\boldsymbol{A}(5,3) = {}& -2\gamma(\gamma - 1)M_\infty^2\mu/R\{(U_y + V_x)\mathcal{D}_x + (l_2V_y + l_0W_z + l_0U_x)\mathcal{D}_y \\ & + (V_z + W_y)\mathcal{D}_z\} + \gamma\rho T_y + (1 - \gamma)P_y,\end{aligned} \tag{D22}$$

$$\begin{aligned}\boldsymbol{A}(5,4) = {}& -2\gamma(\gamma - 1)M_\infty^2\mu/R\{(U_z + W_x)\mathcal{D}_x + (l_2W_z + l_0V_y + l_0U_x)\mathcal{D}_z \\ & + (V_z + W_y)\mathcal{D}_y\} + \gamma\rho T_z + (1 - \gamma)P_z,\end{aligned} \tag{D23}$$

https://doi.org/10.1017/jfm.2025.199 Published online by Cambridge University Press

$$\begin{aligned}\boldsymbol{A}(5,5) =& -i\omega\rho - (\gamma-1)(U\rho_x + V\rho_y + W\rho_z) + \rho U\mathcal{D}_x + \rho V\mathcal{D}_y + \rho W\mathcal{D}_z \\ & - \gamma\mu/(R\,\mathrm{Pr})(\mathcal{D}_{xx} + \mathcal{D}_{yy} + \mathcal{D}_{zz}) - \gamma/(R\,\mathrm{Pr})(\mu_x\mathcal{D}_x + \mu_y\mathcal{D}_y + \mu_z\mathcal{D}_z) \\ & - \gamma/(\mathrm{Pr}\,R)(\mu_{xx} + \mu_{yy} + \mu_{zz}) - \gamma(\gamma-1)M_\infty^2\mu_T/(2R)\Theta, \end{aligned} \tag{D24}$$

$$\boldsymbol{B}(1,1) = UC_x + VC_y + WC_z, \quad \boldsymbol{B}(1,2) = C_x\rho, \quad \boldsymbol{B}(1,3) = C_y\rho, \quad \boldsymbol{B}(1,4) = C_z\rho, \tag{D25}$$

$$\boldsymbol{B}(2,1) = \Omega_{PNS}T/(\gamma M^2)C_x, \quad \boldsymbol{B}(2,2) = \rho(UC_x + VC_y + WC_z), \tag{D26}$$

$$\boldsymbol{B}(2,5) = \Omega_{PNS}\rho/(\gamma M^2)C_x, \quad \boldsymbol{B}(3,1) = T/(\gamma M^2)C_y, \tag{D27}$$

$$\boldsymbol{M}(3,3) = \rho(UC_x + VC_y + WC_z), \quad \boldsymbol{B}(4,1) = T/(\gamma M^2)C_z, \tag{D28}$$

$$\boldsymbol{B}(4,4) = \rho(UC_x + VC_y + WC_z), \tag{D29}$$

$$\boldsymbol{B}(5,1) = -(\gamma-1)(\Omega_{PNS}UC_x + VC_y + WC_z)T, \tag{D30}$$

$$\boldsymbol{B}(5,5) = \rho(UC_x + VC_y + WC_z) + \gamma(1-\Omega_{PNS})\rho UC_x, \tag{D31}$$

where

$$C_x \equiv \frac{\partial\xi}{\partial x}, \quad C_y \equiv \frac{\partial\eta}{\partial y}, \quad C_z \equiv \frac{\partial\phi}{\partial z}, \tag{D32}$$

$$\mathcal{D}_x \equiv i\alpha C_x + \overline{\mathcal{D}}_x, \quad \mathcal{D}_y \equiv i\alpha C_y + \overline{\mathcal{D}}_y, \quad \mathcal{D}_z = i\alpha C_z + \overline{\mathcal{D}}_z, \tag{D33}$$

$$\overline{\mathcal{D}}_x \equiv \frac{\partial\eta}{\partial x}\frac{\partial}{\partial\eta} + \frac{\partial\phi}{\partial x}\frac{\partial}{\partial\phi}, \quad \overline{\mathcal{D}}_y \equiv \frac{\partial\eta}{\partial y}\frac{\partial}{\partial\eta} + \frac{\partial\phi}{\partial y}\frac{\partial}{\partial\phi}, \quad \overline{\mathcal{D}}_z \equiv \frac{\partial\eta}{\partial z}\frac{\partial}{\partial\eta} + \frac{\partial\phi}{\partial z}\frac{\partial}{\partial\phi}. \tag{D34}$$

$$\Theta = \left(\nabla\boldsymbol{V} + \nabla\boldsymbol{V}^t - \frac{2}{3}\nabla\cdot\boldsymbol{V}\boldsymbol{I}\right) : \left(\nabla\boldsymbol{V} + \nabla\boldsymbol{V}^t - \frac{2}{3}\nabla\cdot\boldsymbol{V}\boldsymbol{I}\right). \tag{D35}$$

Appendix E. Entries of linear operators in APSE3D

The non-zero elements of coefficient matrix $\boldsymbol{A}^\dagger$ in (2.41) are as follows:

$$\boldsymbol{A}^\dagger(1,1) = i\omega - U\mathcal{D}_x - V\mathcal{D}_y - W\mathcal{D}_z, \tag{E1}$$

$$\boldsymbol{A}^\dagger(1,2) = UU_x + VU_y + WU_z - \frac{T}{\gamma M_\infty^2}\mathcal{D}_x, \tag{E2}$$

$$\boldsymbol{A}^\dagger(1,3) = UV_x + VV_y + WV_z - \frac{T}{\gamma M_\infty^2}\mathcal{D}_y, \tag{E3}$$

$$\boldsymbol{A}^\dagger(1,4) = UW_x + VW_y + WW_z - \frac{T}{\gamma M_\infty^2}\mathcal{D}_z, \tag{E4}$$

$$\begin{aligned}\boldsymbol{A}^\dagger(1,5) =& -(\gamma-1)i\omega T + \gamma(UT_x + VT_y + WT_z) + (\gamma-1)(U_x + V_y + W_z)T \\ & + (\gamma-1)T(U\mathcal{D}_x + V\mathcal{D}_y + W\mathcal{D}_z), \end{aligned} \tag{E5}$$

$$\boldsymbol{A}^\dagger(2,1) = -\rho\mathcal{D}_x, \tag{E6}$$

https://doi.org/10.1017/jfm.2025.199 Published online by Cambridge University Press

$$\boldsymbol{A}^{\dagger}(2,2) = i\omega\rho - \rho_x U - \rho_y V - \rho V_y - \rho_z W - \rho W_z - (\rho U - l_2\mu_x/R)\mathcal{D}_x - (\rho V - \mu_y/R)\mathcal{D}_y - (\rho W - \mu_z/R)\mathcal{D}_z - \mu/R(l_2\mathcal{D}_{xx} + \mathcal{D}_{yy} + \mathcal{D}_{zz}), \quad \text{(E7)}$$

$$\boldsymbol{A}^{\dagger}(2,3) = \rho V_x - \mu_y/R\mathcal{D}_x - l_0\mu_x/R\mathcal{D}_y - l_1\mu/R\mathcal{D}_x\mathcal{D}_y, \quad \text{(E8)}$$

$$\boldsymbol{A}^{\dagger}(2,4) = \rho W_x - \mu_z/R\mathcal{D}_x - l_0\mu_x/R\mathcal{D}_z - l_1\mu/R\mathcal{D}_x\mathcal{D}_z, \quad \text{(E9)}$$

$$\boldsymbol{A}^{\dagger}(2,5) = \gamma\rho T_x + (1-\gamma)P_x + 2\gamma(\gamma-1)M_\infty^2/R\{\overline{\mathcal{D}}_x(\mu(l_2U_x + l_0V_y + l_0W_z)) + \overline{\mathcal{D}}_y(\mu(U_y + V_x)) + \overline{\mathcal{D}}_z(\mu(U_z + W_x))\} + 2\gamma(\gamma-1)M_\infty^2\mu/R\{(l_2U_x + l_0V_y + l_0W_z)\mathcal{D}_x + (U_y + V_x)\mathcal{D}_y + (U_z + W_x)\mathcal{D}_z\}, \quad \text{(E10)}$$

$$\boldsymbol{A}^{\dagger}(3,1) = -\rho\mathcal{D}_y, \quad \text{(E11)}$$

$$\boldsymbol{A}^{\dagger}(3,2) = \rho U_y - \mu_x/R\mathcal{D}_y - l_0\mu_y/R\mathcal{D}_x - l_1/R\mu\mathcal{D}_x\mathcal{D}_y, \quad \text{(E12)}$$

$$\boldsymbol{A}^{\dagger}(3,3) = i\omega\rho - (\rho_x U + \rho U_x + \rho_y V + \rho W_z + \rho_z W) - (\rho U + \mu_x/R)\mathcal{D}_x - (\rho V + l_2\mu_y/R)\mathcal{D}_y - (\rho W + \mu_z/R)\mathcal{D}_z - \mu/R(\mathcal{D}_{xx} + l_2\mathcal{D}_{yy} + \mathcal{D}_{zz}), \quad \text{(E13)}$$

$$\boldsymbol{A}^{\dagger}(3,4) = \rho W_y - \mu_z/R\mathcal{D}_y - l_0\mu_y/R\mathcal{D}_z - l_1/R\mu\mathcal{D}_y\mathcal{D}_z, \quad \text{(E14)}$$

$$\boldsymbol{A}^{\dagger}(3,5) = \gamma\rho T_y + (1-\gamma)P_y + 2\gamma(\gamma-1)M_e^2/R\{\overline{\mathcal{D}}_y(\mu(l_0U_x + l_2V_y + l_0W_z)) + \overline{\mathcal{D}}_x(\mu(U_y + V_x)) + \overline{\mathcal{D}}_z(\mu(V_z + W_y))\} + 2\gamma(\gamma-1)M_e^2\mu/R\{(l_0U_x + l_2V_y + l_0W_z)\mathcal{D}_y + (U_y + V_x)\mathcal{D}_x + (V_z + W_y)\mathcal{D}_z\}, \quad \text{(E15)}$$

$$\boldsymbol{A}^{\dagger}(4,1) = -\rho\mathcal{D}_z, \quad \text{(E16)}$$

$$\boldsymbol{A}^{\dagger}(4,2) = \rho U_z - \mu_x/R\mathcal{D}_z - l_0\mu_z/R\mathcal{D}_x - l_1/R\mu\mathcal{D}_x\mathcal{D}_z, \quad \text{(E17)}$$

$$\boldsymbol{A}^{\dagger}(4,3) = \rho V_z - \mu_y/R\mathcal{D}_z - l_0\mu_z/R\mathcal{D}_y - l_1/R\mu\mathcal{D}_y\mathcal{D}_z, \quad \text{(E18)}$$

$$\boldsymbol{A}^{\dagger}(4,4) = i\omega\rho - (\rho_x U + \rho U_x + \rho V_y + \rho_y V + \rho_z W) - (\rho U + \mu_x/R)\mathcal{D}_x - (\rho V + \mu_y/R)\mathcal{D}_y - (\rho W + l_2\mu_z/R)\mathcal{D}_z - \mu/R(\mathcal{D}_{xx} + \mathcal{D}_{yy} + l_2\mathcal{D}_{zz}), \quad \text{(E19)}$$

$$\boldsymbol{A}^{\dagger}(4,5) = \gamma\rho T_z + (1-\gamma)P_z + 2\gamma(\gamma-1)M_\infty^2/R\{\overline{\mathcal{D}}_z(\mu(l_0U_x + l_0V_y + l_2W_z)) + \overline{\mathcal{D}}_y(\mu(W_y + V_z)) + \overline{\mathcal{D}}_x(\mu(U_z + W_x))\} + 2\gamma(\gamma-1)M_e^2\mu/R\{(l_0U_x + l_0V_y + l_2W_z)\mathcal{D}_z + (W_y + V_z)\mathcal{D}_y + (U_z + W_x)\mathcal{D}_x\}, \quad \text{(E20)}$$

$$\boldsymbol{A}^{\dagger}(5,1) = 0, \quad \text{(E21)}$$

$$\boldsymbol{A}^{\dagger}(5,2) = -\rho/(\gamma M_\infty^2)\mathcal{D}_x + \mu_T/R\left\{(l_2U_x + l_0V_y + l_0W_z)\mathcal{D}_x + (U_y + V_x)\mathcal{D}_y + (U_z + W_x)\mathcal{D}_z\right\}, \quad \text{(E22)}$$

$$\boldsymbol{A}^{\dagger}(5,3) = -\rho/(\gamma M_\infty^2)\mathcal{D}_y + \mu_T/R\{(l_0U_x + l_2V_y + l_0W_z)\mathcal{D}_y + (U_y + V_x)\mathcal{D}_x + (V_z + W_y)\mathcal{D}_z\}, \quad \text{(E23)}$$

https://doi.org/10.1017/jfm.2025.199 Published online by Cambridge University Press

$$\boldsymbol{A}^{\dagger}(5,4) = -\rho/(\gamma M_{\infty}^2)\mathcal{D}_z + \mu_T/R\{(l_0U_x + l_0V_y + l_2W_z)\mathcal{D}_z + (W_y + V_z)\mathcal{D}_y + (U_z + W_x)\mathcal{D}_x\}, \tag{E24}$$

$$\begin{aligned}\boldsymbol{A}^{\dagger}(5,5) = {} & i\omega\rho - \gamma(U\rho_x + V\rho_y + W\rho_z) - \rho(U_x + V_y + W_z) \\ & - \gamma\mu/(\mathrm{Pr}\,R)(\mathcal{D}_{xx} + \mathcal{D}_{yy} + \mathcal{D}_{zz}) - \gamma/(R\,\mathrm{Pr})(\mu_x\mathcal{D}_x + \mu_y\mathcal{D}_y + \mu_z\mathcal{D}_z) \\ & - \gamma/(\mathrm{Pr}\,R)(\mu_{xx} + \mu_{yy} + \mu_{zz}) - \gamma(\gamma - 1)M_{\infty}^2\mu_T/(2R)\Theta.\end{aligned} \tag{E25}$$

$$\boldsymbol{B}^{\dagger} = \boldsymbol{B}^{tr}. \tag{E26}$$

References

Åkervik, E., Ehrenstein, U., Gallarire, F. & Henningson, D.S. 2008 Global two-dimensional stability measures of the flat plate boundary layer flow. *Eur. J. Mech B* **27** (5), 501–513.

Alizard, F. & Robinet, J.-C. 2007 Spatially convective global modes in a boundary layer. *Phys. Fluids* **19**, 114105.

Araya, D. *et al.* 2023 Linear analysis of boundary-layer instabilities on a finned-cone at Mach 6. https://arxiv.org/abs/2303.10747 (preprint).

Bagheri, S., Åkervik, E., Brandt, L. & Henningson, D.S. 2009 Matrix-free methods for the stability and control of boundary layers. *AIAA J.* **47** (5), 1057–1068.

Bippes, H. 1999 Basic experiments on transition in three-dimensional boundary layers dominated by crossflow instability. *Prog. Aerosp. Sci.* **35** (4), 363–412.

Butler, K.M. & Farrell, B.F. 1992 Three-dimensional optimal perturbations in viscous shear flow. *Phys. Fluids* **4** (8), 1637–1650.

Chen, X., Dong, S., Tu, G., Yuan, X. & Chen, J. 2022 Boundary layer transition and linear modal instabilities of hypersonic flow over a lifting body. *J. Fluid Mech.* **938**, A8.

Chen, X., Dong, S., Tu, G., Yuan, X. & Chen, J. 2023 Global stability analyses of Mack mode on the windward face of a hypersonic yawed cone. *Phys. Rev. Fluids* **8**, 033903.

Chen, X., Tu, G., Wan, B., Yuan, X., Chen, J. & Chen, J. 2024 The leeward vortex transition over hypersonic yawed cones by eN method based on global stability theory (in Chinese). *Acta Aerodyn. Sin.* **42** (1), 33–44.

Chen, X., Zhu, Y. & Lee, C. 2017 Interactions between second mode and low-frequency waves in a hypersonic boundary layer. *J. Fluid Mech.* **820**, 693–735.

Chomaz, J. 2005 Global instabilities in spatially developing flows: non-normality and nonlinearity. *Annu. Rev. Fluid Mech.* **37** (1), 357–392.

Chu, B.T. 1965 On the energy transfer to small disturbances in fluid flow (part 1). *Acta Mechanica* **1** (3), 215–234.

Cook, D., Knutson, A. & Nichols, J. 2020 Matrix methods for input-output analysis of 2D and 3D hypersonic flows. *AIAA Paper 2020-1820*. AIAA.

Corbett, P. & Bottaro, A. 2001 Optimal linear growth in swept boundary layers. *J. Fluid Mech.* **435**, 1–23.

Corke, T., Arndt, A., Matlis, E. & Semper, M. 2018 Control of stationary cross-flow modes in a Mach 6 boundary layer using patterned roughness. *J. Fluid Mech.* **856**, 822–849.

Cossu, C. & Chomaz, J.M. 1997 Global measures of local convective instabilities. *Phys. Rev. Lett.* **78** (23), 4387–4390.

Dobrinsky, A. 2002 Adjoint analysis for receptivity prediction. PhD thesis, Rice University, USA.

Ehrenstein, U. & Gallaire, F. 2005 On two-dimensional temporal modes in spatially evolving open flows: the flat-plate boundary layer. *J. Fluid Mech.* **536**, 209–218.

Farrell, B.F. & Ioannou, P.J. 1993 Optimal excitation of three-dimensional perturbations in viscous constant shear flow. *Phys. Fluids* **5** (6), 1390–1400.

Giannetti, F. & Luchini, P. 2007 Structural sensitivity of the first instability of the cylinder wake. *J. Fluid Mech.* **581** (1), 167–197.

Guegan, A., Schmid, P.J. & Huerre, P. 2008 Spatial optimal disturbances in swept attachment-line boundary layers. *J. Fluid Mech.* **603**, 179–188.

Hanifi, A., Schmid, P.J. & Henningson, D.S. 1996 Transient growth in compressible boundary layer flow. *Phys. Fluids* **8** (3), 826–837.

Jovanović, M.R. & Bamieh, B. 2005 Componentwise energy amplification in channel flows. *J. Fluid Mech.* **534**, 145–183.

https://doi.org/10.1017/jfm.2025.199 Published online by Cambridge University Press

KOCIAN, T.S., MOYES, A.J., REED, H.L., CRAIG, S.A., SARIC, W.S., SCHNEIDER, S.P. & EDELMAN, J.B. 2019 Hypersonic crossflow instability. *J. Spacecr. Rockets* **56** (2), 432–446.
LAIBLE, A.C. & FASEL, H.F. 2016 Continuously forced transient growth in oblique breakdown for supersonic boundary layers. *J. Fluid Mech.* **804**, 323–350.
LAKEBRINK, M.T., PAREDES, P. & BORG, M.P. 2017 Toward robust prediction of crossflow-wave instability in hypersonic boundary layers. *Comput. Fluids* **144**, 1–9.
LEVIN, O. & HENNINGSON, D.S. 2003 Exponential vs algebraic growth and transition prediction in boundary layer flow. *Flow, Turbul. Combust.* **70** (1-4), 183–210.
LI, F., CHOUDHARI, M., CHANG, C.-L. & WHITE, J. 2010 Analysis of instabilities in non-axisymmetric hypersonic boundary layers over cones. *AIAA Paper 2010-4643*. AIAA.
LI, X., CHEN, J., HUANG, Z., YANG, Q. & XU, G. 2020 Stability analysis and transition prediction of streamwise vortices over a yawed cone at Mach 6. *Phys. Fluids* **32**, 124110.
LIU, S., CHEN, X., WAN, B., ZHANG, L. & CHEN, J. 2024 Nonmodal linear stability analysis of hypersonic flow over an inclined cone. *Phys. Fluids* **36**, 084107.
LIU, S., WAN, B., YUAN, X., ZHANG, L., CHEN, J. & CHEN, X. 2022*a* Linear modal global instabilities of hypersonic flow over an inclined cone. *Phys. Fluids* **34**, 074108.
LIU, Y., SCHUABB, M., DUAN, L., PAREDES, P. & CHOUDHARI, M.M. 2022*b* Interaction of a tunnel-like acoustic disturbance field with a blunt cone boundary layer at Mach 8. *AIAA Paper 2022-3250*. AIAA.
LUCHINI, P. 2000 Reynolds-number-independent instability of the boundary layer over a flat surface: optimal perturbations. *J. Fluid Mech.* **404**, 289–309.
NASTRO, G., FONTANE, J. & JOLY, L. 2020 Optimal perturbations in viscous round jets subject to Kelvin–Helmholtz instability. *J. Fluid Mech.* **900**, A13.
NICHOLS, J.W. & LELE, S.K. 2011 Global modes and transient response of a cold supersonic jet. *J. Fluid Mech.* **669**, 225–241.
PAREDES, P., CHOUDHARI, M. & LI, F. 2020 Mechanism for frustum transition over blunt cones at hypersonic speeds. *J. Fluid Mech.* **894**, A22.
PAREDES, P., CHOUDHARI, M., LI, F. & CHANG, C.-L. 2016*a* Optimal growth in hypersonic boundary layers. *AIAA J.* **54** (10), 3050–3061.
PAREDES, P., CHOUDHARI, M., LI, F., JEWELL, J.S. & KIMMEL, R.L. 2019 Nonmodal growth of traveling waves on blunt cones at hypersonic speeds. *AIAA Paper 2019-0876*. AIAA.
PAREDES, P., GOSSE, R., THEOFILIS, V. & KIMMEL, R. 2016*b* Linear modal instabilities of hypersonic flow over an elliptic cone. *J. Fluid Mech.* **804**, 442–466.
PAREDES, P., SCHOLTEN, A., CHOUDHARI, M. & LI, F. 2023 Modal instabilities over blunted cones at angle of attack in hypersonic flow. *J. Spacecr. Rockets* **60** (4), 1188–1200.
PAREDES, P., SCHOLTEN, A., CHOUDHARI, M., LI, F., PRICE, B. & JEWELL, J. 2022 Combined bluntness and roughness effects on cones at hypersonic speeds. *AIAA 2022-3340*. AIAA.
QUINTANILHA, H., PAREDES, P. & HANIFI, A. 2022 Transient growth analysis of hypersonic flow over an elliptic cone. *J. Fluid Mech.* **935**, A40.
REDDY, S., SCHMID, P.J. & HENNINGSON, D.S. 1993 Pseudospectra of the Orr–Sommerfeld Operator. *SIAM J. Appl. Maths* **53** (1), 15–47.
REED, H.L. & SARIC, W.S. 1989 Stability of three-dimensional boundary layers. *Ann. Rev. Fluid Mech.* **21** (1), 235–284.
RESHOTKO, E. & TUMIN, A. 2000 The blunt body paradox – a case for transient growth. In *Laminar-Turbulence Transition, IUTAM Symposium, Sedona* (ed. H.F. FASEL & W.S. SARIC), pp. 403–408, Springer-Verlag.
SCHMID, P.J. 2007 Nonmodal stability theory. *Annu. Rev. Fluid Mech.* **39** (1), 129–162.
SCHMID, P.J. & BRANDT, L. 2014 Analysis of fluid systems: stability, receptivity, sensitivity: lecture notes from the FLOW-NORDITA summer school on advanced instability methods for complex flows. *Appl. Mech. Rev.* **66**, 024803.
SCHMID, P.J. & HENNINGSON, D.S. 2001 *Stability and Transition in Shear Flows*. Springer-Verlag.
SCHUABB, M., DUAN, L., SCHOLTEN, A., PAREDES, P. & CHOUDHARI, M.M. 2024 Hypersonic boundary-layer transition over a blunt circular cone in a Mach 8 digital wind tunnel. *AIAA Paper 2024-2181*. AIAA.
SCHUELE, C.-Y., CORKE, T. & MATLIS, E. 2013 Control of stationary cross-flow modes in a Mach 3.5 boundary layer using patterned passive and active roughness. *J. Fluid Mech.* **718**, 5–38.
SKENE, C.S., YEH, C.-A., SCHMID, P.J. & TAIRA, K. 2022 Sparsifying the resolvent forcing mode via gradient-based optimisation. *J. Fluid Mech.* **944**, A52.
SONG, R., ZHAO, L. & HUANG, Z. 2020 Improvement of the parabolized stability equation to predict the linear evolution of disturbances in three-dimensional boundary layers based on ray tracing theory. *Phys. Rev. Fluids* **5**, 033901.

https://doi.org/10.1017/jfm.2025.199 Published online by Cambridge University Press

SWANSON, E. & SCHNEIDER, S. 2010 Boundary-layer transition on cones at angle of attack in a Mach-6 quiet tunnel. *AIAA Paper 2010-1062*. AIAA.

TEMPELMANN, D., HANIFI, A. & HENNINGSON, D.S. 2010 Spatial optimal growth in three-dimensional boundary layers. *J. Fluid Mech.* **646**, 5–37.

TEMPELMANN, D., HANIFI, A. & HENNINGSON, D.S. 2012 Spatial optimal growth in three-dimensional compressible boundary layers. *J. Fluid Mech.* **704**, 251–279.

TOWNE, A., RIGAS, G. & COLONIUS, T. 2019 A critical assessment of the parabolized stability equations. *Theor. Comput. Fluid Dyn.* **33**, 359–382.

TREFETHEN, L. & EMBREE, M. 2005 *Spectra and Pseudospectra*. Princeton University Press.

TUMIN, A. & RESHOTKO, E. 2001 Spatial theory of optimal disturbances in boundary layers. *Phys. Fluids* **13** (7), 2097–2104.

TUMIN, A. & RESHOTKO, E. 2003 Optimal disturbances in compressible boundary layers. *AIAA J.* **41** (12), 2357–2363.

VIGNERON, Y., RAKICH, J. & TANNEHILL, J. 1978 Calculation of supersonic viscous flow over delta wings with sharp supersonic leading edges. *AIAA Paper 1978-1137*. AIAA.

WAN, B., LUO, J. & SU, C. 2018 Response of a hypersonic blunt cone boundary layer to slow acoustic waves with assessment of various routes of receptivity. *Appl. Maths Mech.* **39** (11), 1643–1660.

WANG, Q., XIANG, X., DONG, S., YUAN, X., CHEN, J. & CHEN, X. 2023 Wall temperature effects on the hypersonic boundary-layer transition over an inclined blunt cone. *Phys. Fluids* **35**, 024107.

WASSERMANN, P. & KLOKER, M. 2003 Transition mechanisms induced by travelling crossflow vortices in a three-dimensional boundary layer. *J. Fluid Mech.* **483**, 67–89.

ZHANG, L., CHEN, X., LIU, S., WANG, Q., DONG, S., DUAN, M. & CHEN, J. 2025 Transition front prediction for the HyTRV model based on multi-dimensional stability theories. *Adv. Aerodyn.* **7**, https://doi.org/10.1186/s42774-024-00202-3 (in press).

ZHAO, L. 2017 Study on instability of stationary crossflow vortices in hypersonic swept blunt plate boundary layers. PhD thesis, Tianjin University, China.

https://doi.org/10.1017/jfm.2025.199 Published online by Cambridge University Press